Supporting Information

Coinage metal(I) clusters supported by a 1,10-phenanthroline-phosphine: orange-to-NIR phosphorescence, metallophilic interactions and enhanced cytotoxicity

Alexander V. Artem'ev,*[a] Maria P. Davydova,[a] Lyubov S. Klyushova,[b] Evgeniy H. Sadykov,[a] Mariana I. Rakhmanova,[a] Taisiya S. Sukhikh[a]

[a] *Nikolaev Institute of Inorganic Chemistry, SB RAS, 3, Lavrentiev Ave., 630090 Novosibirsk, Russia*
[b] *Institute of Molecular Biology and Biophysics, Federal Research Center of Fundamental and Translational Medicine, Timakova Str. 2/12, 630060 Novosibirsk, Russia*

*E-mail: chemisufarm@yandex.ru (Alexander V. Artem'ev)

Table of content

§1. Materials and Instrumentation

2-Chloro-1,10-phenanthroline (>98.0%, TCI), *n*-buthyllithium (2.5 M in hexanes, Sigma-Aldrich), diphenylphosphine (98%, Sigma-Aldrich), CuI (99%, Sigma-Aldrich), $AgBF_4$ (≥ 98.0 %, Sigma-Aldrich), $[Ag(MeCN)_4]PF_6$ (97%, Sigma-Aldrich), $[Cu(MeCN)_4]PF_6$ (97%, Sigma-Aldrich) and $[Cu(MeCN)_4]BF_4$ (97%, Sigma-Aldrich) were used as purchased. Au(tht)Cl was prepared following the known method.[1] THF (Vekton), MeCN (Cryochrom), MeOH (Vekton), CH_2Cl_2 (ANT), Et_2O (Cryochrom) and Me_2CO (Cryochrom) prior to use were purified by common methods. Synthesis of 2-(diphenylphosphino)-1,10-phenanthroline was carried out under an argon atmosphere, while the complexes **1**–**5** were prepared under ambient conditions.

^1H and $^{31}P\{^1H\}$ NMR spectra were registered using a Bruker AV-500 spectrometer at 500.13 and 202.46 MHz, respectively, with solvent peaks as reference (for ^1H NMR), at room temperature. The $^{31}P\{^1H\}$ NMR shifts are referenced respective to 85% H_3PO_4/D_2O as an external standard.

The microanalyses were performed on a MICRO cube analyzer.

Thermogravimetric analysis (TGA/DTA) was carried out under argon flow at 10 °C/min^{-1} heating rate using a NETZSCH STA 449 F1 Jupiter STA up to 600 °C in a closed Al_2O_3 pan.

ESI-MS spectra were recorded on the Shimadzu LCMS-9030 instrument using direct injection of a MeCN solution (10^{-3} M) of the sample.

UV-Vis absorption spectra were registered on a SF-2000 spectrophotometer (OKB Spectr) for solutions in MeCN (10^{-5} mol·L^{-1}, 298 K).

FT-IR spectra were recorded for pellets with KBr on a Bruker Vertex 80 spectrometer at ambient temperature.

Steady-state excitation and emission spectra were recorded at 298 K on a Fluorolog 3 spectrometer (Horiba Jobin Yvon) equipped with a cooled PC177CE-010 photon detection module and an R2658 photomultiplier. The emission decays were recorded on the same instrument. The absolute PLQYs were determined at 298 K using a Fluorolog 3 Quanta-phi integrating sphere.

§2. Single crystal X-ray crystallography

Single crystals of **1**·4MeCN were obtained by slow evaporation of a CH_3CN solution at room temperature. Single crystals of **2**·3CH_2Cl_2 and **4**·2CH_2Cl_2·H_2O were obtained by vapor diffusion of Et_2O into CH_2Cl_2 solutions. Single crystals of **3** and **5**·0.5Et_2O were obtained by vapor diffusion of Et_2O into MeCN and Me_2CO solutions, respectively.

The data were collected with a Bruker D8 Venture diffractometer with a CMOS PHOTON III detector and IμS 3.0 source (mirror optics, λ(MoKα) = 0.71073 Å). Absorption corrections were applied with the use of the SADABS program[2]. The structures were solved by dual space algorithm (SHELXT[3]) and refined by the full-matrix least squares technique (SHELXL[4]) in the anisotropic approximation (except hydrogen atoms). Positions of hydrogen atoms were calculated geometrically and refined in the riding model.

The crystallographic data and details of the structure refinements are summarized in **Table S1**. CCDC 2239197−2239201 contain the supplementary crystallographic data for this paper. These data can be obtained free of charge from The Cambridge Crystallographic Data Center at http://www.ccdc.cam.ac.uk/data_request/cif

Table S1. X-Ray crystallographic data for **1**−**5**.

Compound	**1**·4MeCN	**2**·3CH_2Cl_2	**3**
CCDC number	2239197	2239200	2239199
Chemical formula	$C_{104}H_{80}Cu_6I_6N_{12}P_4$	$C_{51}H_{40}CuAu_2N_4P_2Cl_8BF_4$	$C_{48}H_{34}AuCuN_4P_4F_{12}$
M_r	2764.32	1598.69	1279.18
Crystal system, space group	Triclinic, $P\bar{1}$	Monoclinic, $C2/c$	Monoclinic, $C2/c$
Temperature (K)	150	150	150
a, b, c (Å)	15.6344(11), 17.6663(13), 21.4428(14)	11.7266(10), 30.047(2), 15.8840(11)	26.5931(14), 8.6249(5), 22.9847(13)
α, β, γ (°)	70.318(2), 78.179(2), 66.302(2)	96.046(3)	119.480(2)
V (Å^3)	5089.7(6)	5565.6(7)	4589.3(5)
Z	2	4	4
μ (mm^{-1})	3.17	6.13	3.89
Crystal size (mm)	0.17 × 0.15 × 0.07	0.23 × 0.13 × 0.05	0.19 × 0.16 × 0.15
T_{min}, T_{max}	0.613, 0.745	0.502, 0.746	0.620, 0.746
No. of measured, independent and observed [$I > 2\sigma(I)$] reflections	59880, 20768, 16343	31582, 6674, 5725	28560, 5478, 5099
R_{int}	0.049	0.051	0.040
$(\sin\theta/\lambda)_{max}$ (Å^{-1})	0.626	0.659	0.658
$R[F^2 > 2\sigma(F^2)]$, $wR(F^2)$, S	0.044, 0.112, 1.02	0.042, 0.111, 1.07	0.022, 0.047, 1.03
No. of reflections	20768	6674	5478
No. of parameters	1193	309	381
No. of restraints	6	4	316
$\Delta\rho_{max}$, $\Delta\rho_{min}$ (e Å^{-3})	1.72, −1.63	1.43, −1.80	0.39, −0.29

Table S1 (continuation). X-Ray crystallographic data for complexes **1**−**5**.

Compound	**4**·2CH_2Cl_2·H_2O	**5**·0.5Et_2O
CCDC number	2239198	2239201
Chemical formula	$C_{50}H_{40}AgAu_2N_4OP_2Cl_6BF_4$	$C_{74}H_{56}AgAuN_6O_{0.5}P_5F_{12}$
M_r	1576.11	1724.89
Crystal system, space group	Monoclinic, *C*2/c	Trigonal, $P\bar{3}$
Temperature (K)	150	150
a, *b*, *c* (Å)	12.1888(8), 30.073(3), 15.7516(11)	15.4928(6), 34.400(3)
α, β, γ (°)	97.452(2)	–
V (Å^3)	5725.1(7)	7150.7(8)
Z	4	4
μ (mm^{-1})	5.84	2.51
Crystal size (mm)	0.2 × 0.15 × 0.08	0.27 × 0.22 × 0.15
T_{min}, T_{max}	0.540, 0.745	0.669, 0.746
No. of measured, independent and observed [$I > 2\sigma(I)$] reflections	29579, 5468, 4724	40745, 9780, 8570
R_{int}	0.096	0.036
$(\sin\theta/\lambda)_{max}$ (Å^{-1})	0.612	0.625
$R[F^2 > 2\sigma(F^2)]$, $wR(F^2)$, *S*	0.060, 0.153, 1.12	0.053, 0.139, 1.08
No. of reflections	5468	9780
No. of parameters	304	591
No. of restraints	25	3
$\Delta\rho_{max}$, $\Delta\rho_{min}$ (e Å^{-3})	2.02, −1.17	4.02, −2.46

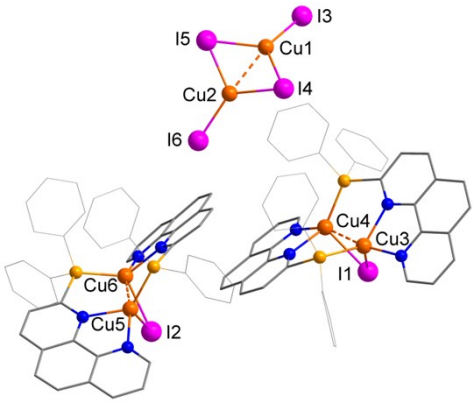

Figure S1. Molecular structure of **1**·4MeCN determined by sc-XRD analysis (the H atoms and solvent molecules are omitted). Selected bond lengths (Å) and angles (°): Cu1···Cu2 2.6235(10), Cu3···Cu4 2.8373(8), Cu5···Cu6 2.8387(8), I3–Cu1 2.5911(9), I6–Cu2 2.4833(14), I4–Cu2 2.5692(11), I5–Cu1 2.5753(9), I2–Cu6 2.6495(7), I5–Cu2 2.5857(11), I2–Cu5 2.6522(7), I1–Cu4 2.6629(7), I1–Cu3 2.6281(7); Cu2–I4–Cu1 61.11(3), I6–Cu2–I4 116.49(11), I6–Cu2–I5 130.29(11), I5–Cu1–I4 112.25(3), Cu6–I2–Cu5 64.71(2), Cu3–I1–Cu4 64.889(19).

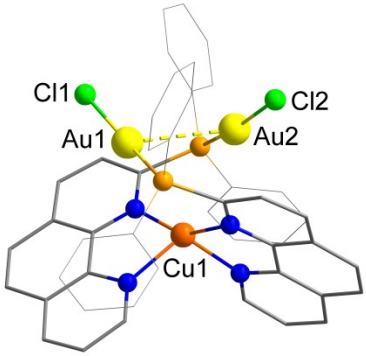

Figure S2. Molecular structure of **2**·3CH_2Cl_2 determined by sc-XRD analysis (the H atoms, BF_4^- counterions and solvent molecules are omitted). Selected bond lengths (Å) and angles (°): Au1···Au2 3.4919(5), Au1–P1 2.2195(15), Au1–Cl1 2.2873(15); Cl1–Au1···Au2 92.99(4), P1–Au1–Cl1 169.94(6), P1–Au1···Au2 93.41(4).

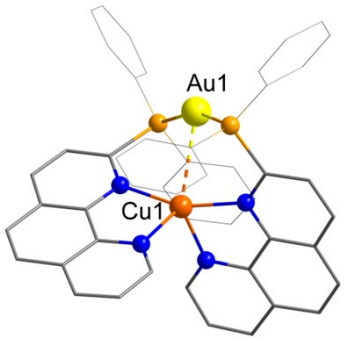

Figure S3. Molecular structure of **3** determined by sc-XRD analysis (the H atoms, PF_6^- counterions are omitted). Selected bond lengths (Å) and angles (°): Au1···Cu1 2.8690(4), Au1–P1 2.3020(6), Au1–P2 2.3019(5); P2–Au1···Cu1 80.290(14), P2–Au1–P1 160.58(3); P1–Au1···Cu1 80.291(14).

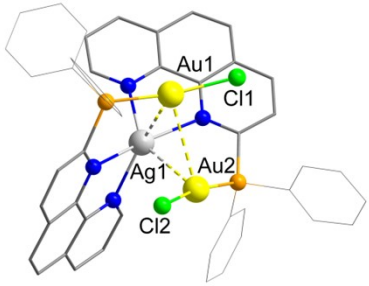

Figure S4. Molecular structure of **4**·2CH_2Cl_2·H_2O determined by sc-XRD analysis (the H atoms, BF_4^- counterions and solvent molecules are omitted). Selected bond lengths (Å) and angles (°): Au1···Au2 3.3059(8), Au1···Ag1 3.1030(11), Au1–P1 2.233(3), Au1–Cl1 2.289(3); Ag1···Au1···Au2 57.813(15), P1–Au1···Ag1 79.58(7), Cl1–Au1···Au2 88.63(7), P1–Au1–Cl1 168.70(10), Cl1–Au1···Ag1 111.37(8), Au2···Ag1···Au1 64.37(3), P1–Au1···Au2 100.03(7).

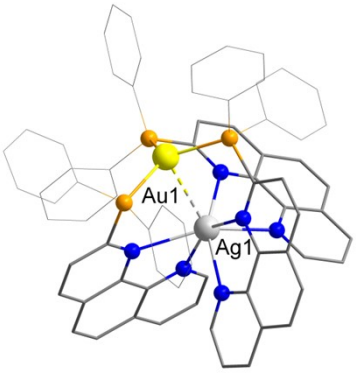

Figure S5. Molecular structure of **5**·0.5Et_2O determined by sc-XRD analysis (the H atoms, PF_6^- counterions and solvent molecules are omitted). Selected bond lengths (Å) and angles (°): Au1···Ag1 2.9294(12), Au1–P1 2.3575(18), Au1–P2 2.3575(19), Au1–P3 2.3576(18); P2–Au1···Ag1 88.82(5), P3–Au1···Ag1 88.82(5), P1–Au1···Ag1 88.82(5), P1–Au1–P3 119.957(4); P2–Au1–P3 9.956(4).

§3. ^1H and $^{31}P\{^1H\}$ NMR spectra

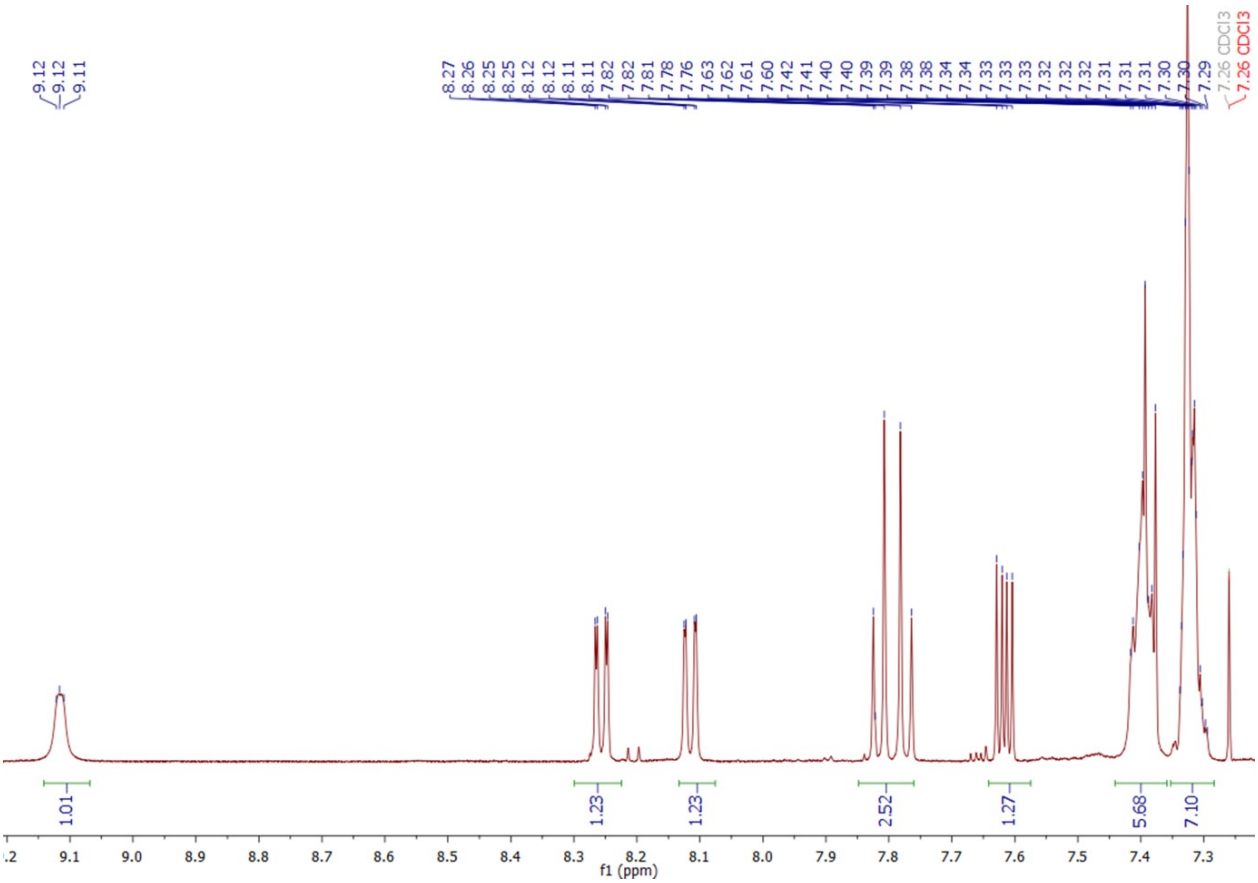

Figure S6. ^1H NMR spectrum of **L** ($CDCl_3$), selected range.

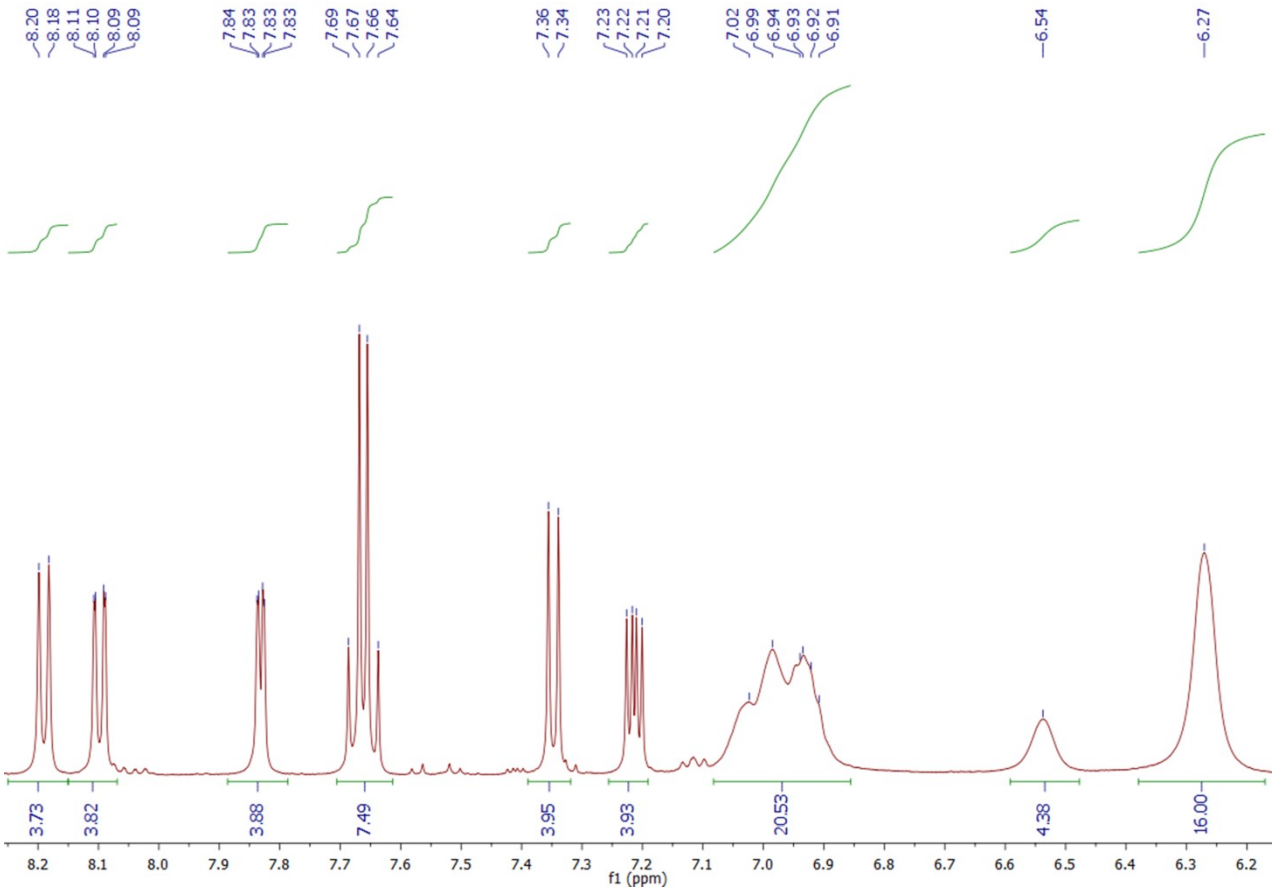

Figure S7. ^{1}H NMR spectrum of **1** (DMSO-d_6), selected range.

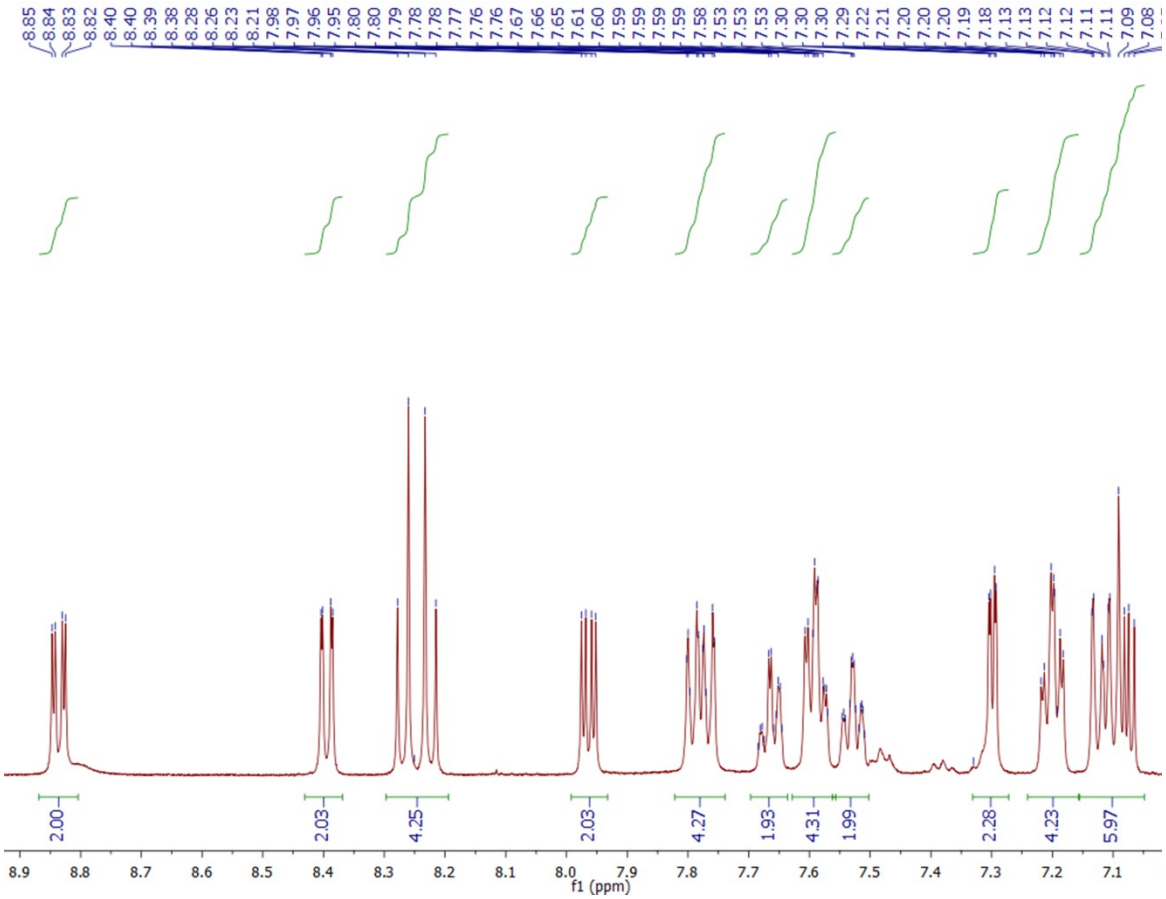

Figure S8. ^{1}H NMR spectrum of **2** (CD_3CN), selected range.

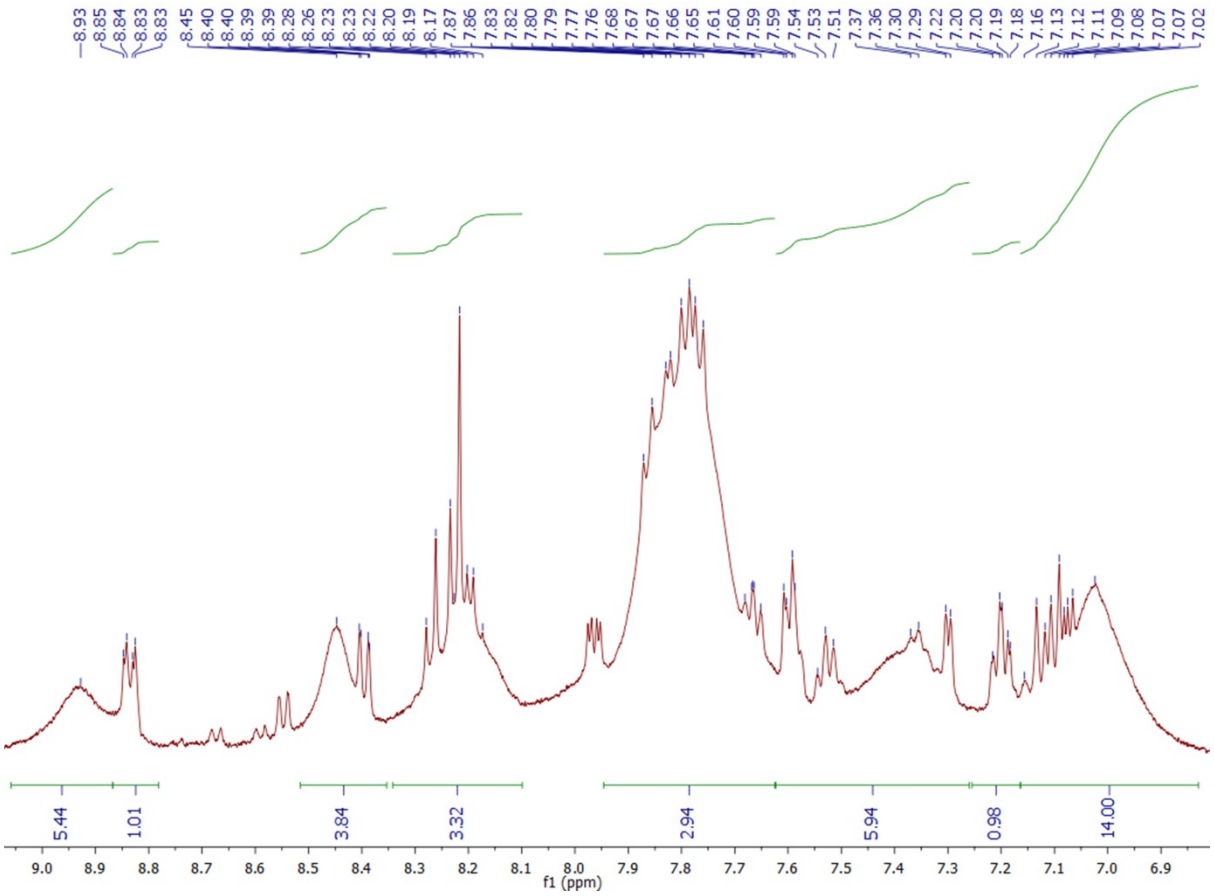

Figure S9. ^{1}H NMR spectrum of **3** (CD_3CN), selected range.

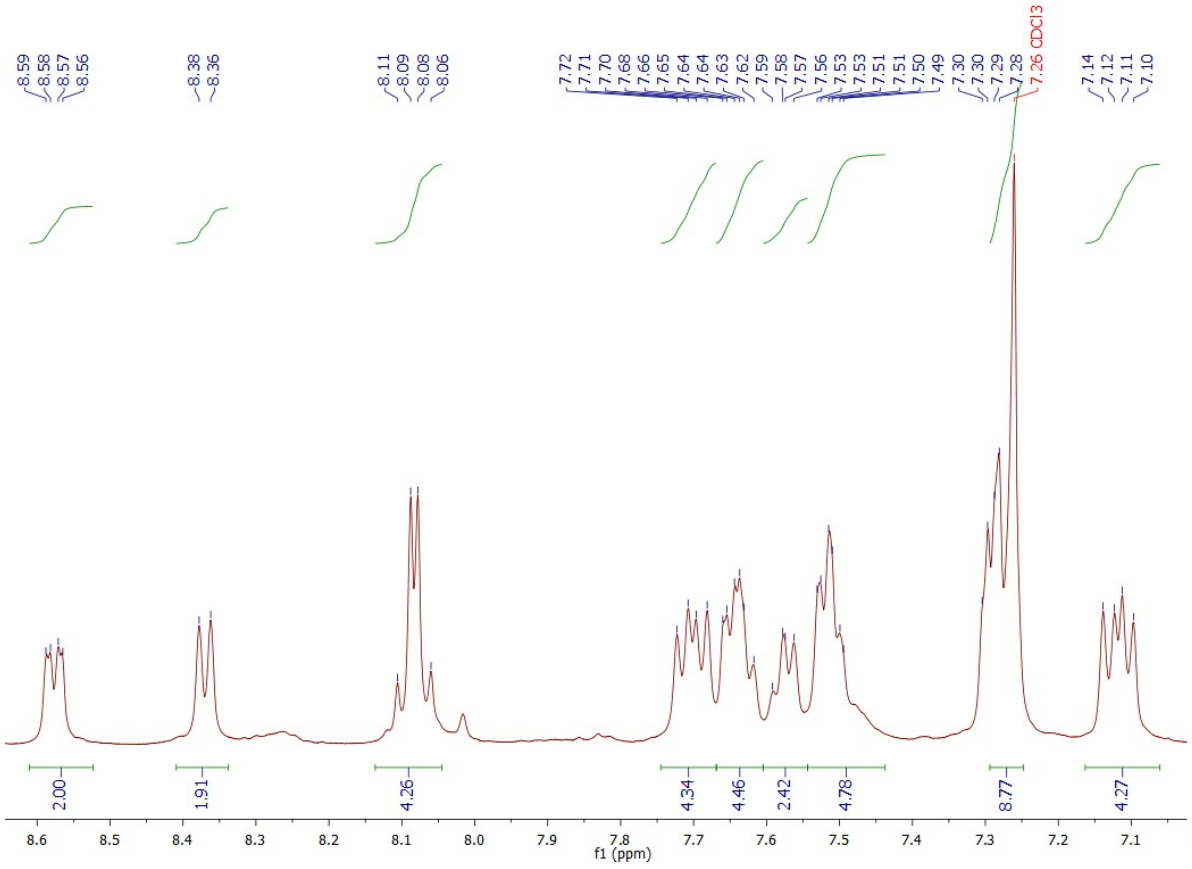

Figure S10. ^{1}H NMR spectrum of **4** ($CDCl_3$), selected range.

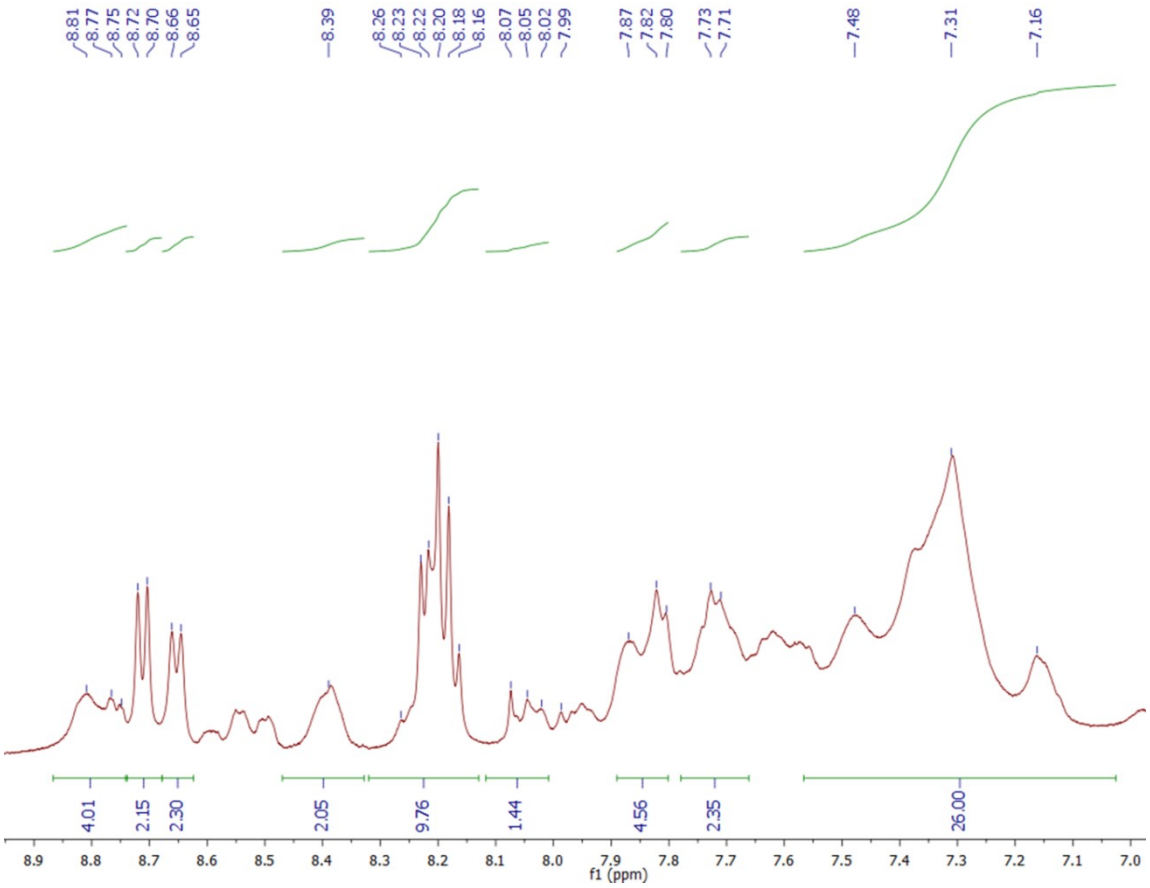

Figure S11. ^{1}H NMR spectrum of **5** (CD_3CN), selected range.

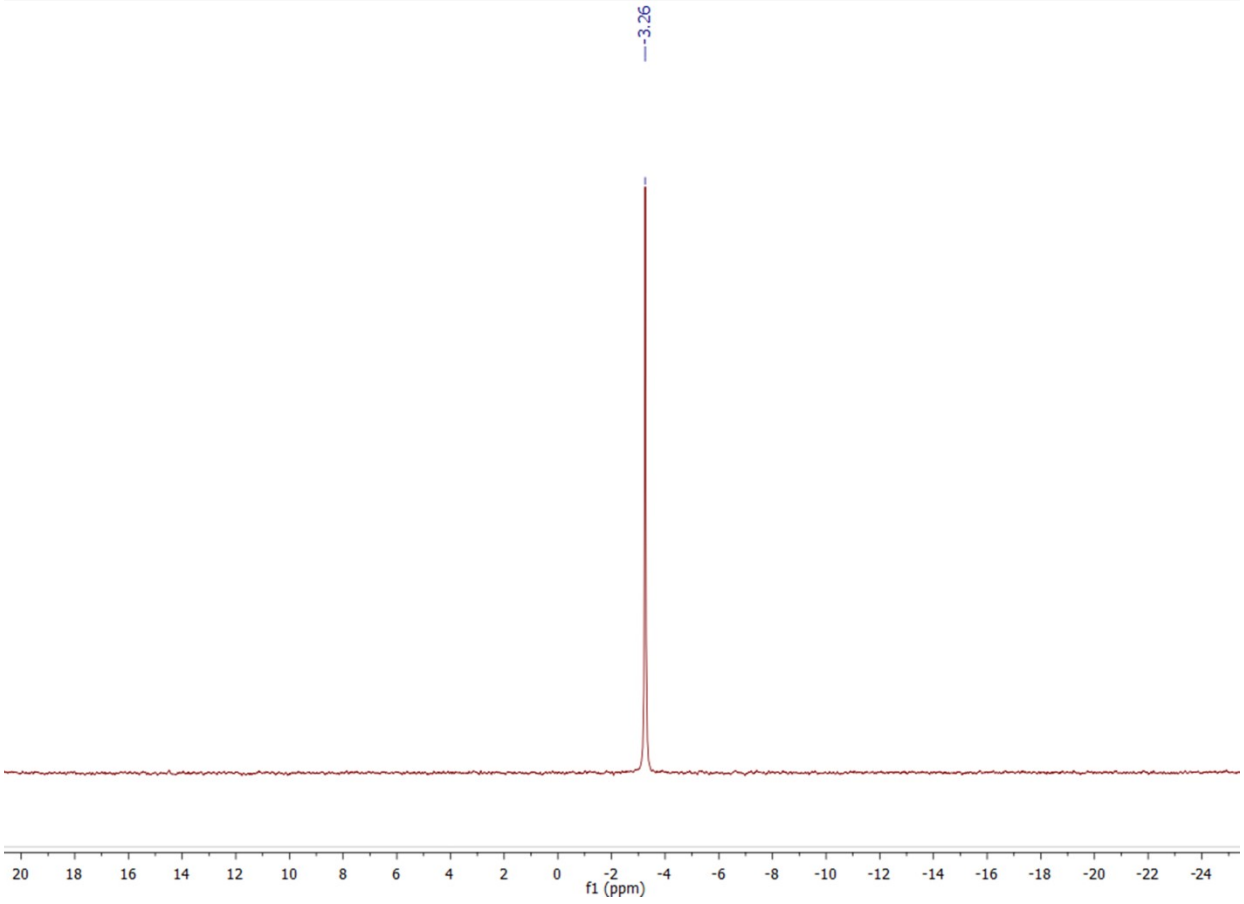

Figure S12. $^{31}P\{^{1}H\}$ NMR spectrum of **L** ($CDCl_3$), selected range.

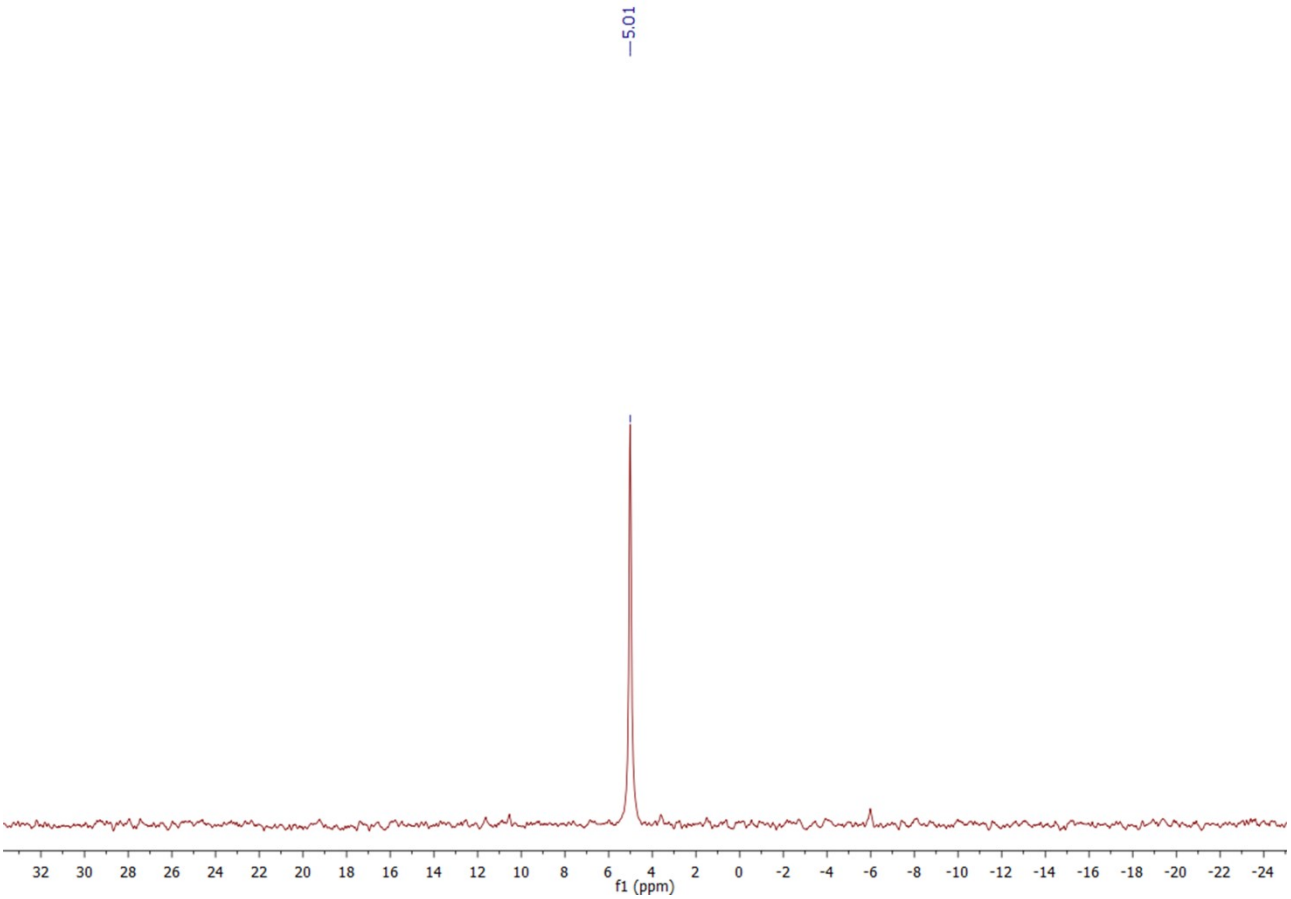

Figure S13. $^{31}P\{^{1}H\}$ NMR spectrum of **1** (DMSO-d_6), selected range.

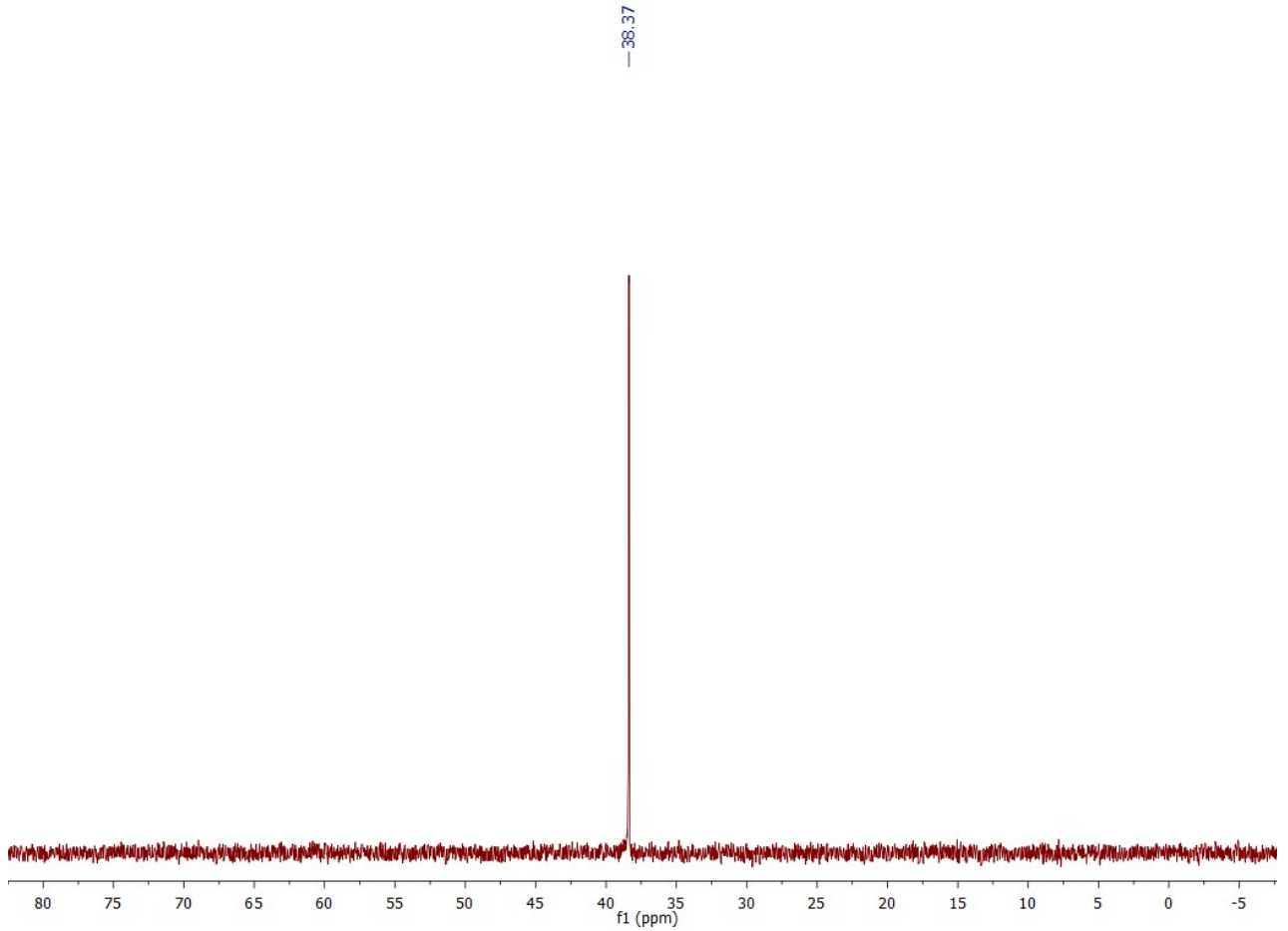

Figure S14. $^{31}P\{^{1}H\}$ NMR spectrum of **2** (CD_3CN), selected range.

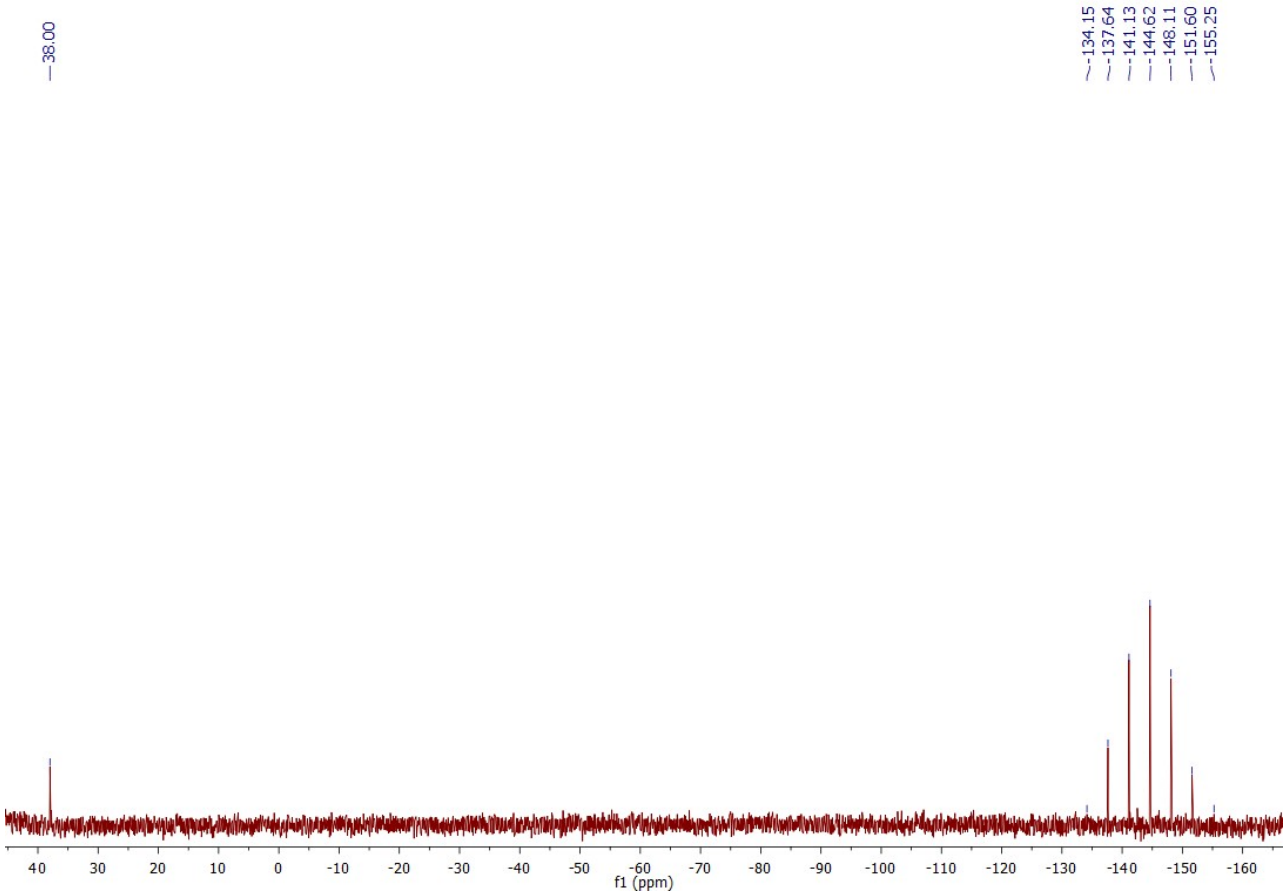

Figure S15. $^{31}P\{^{1}H\}$ NMR spectrum of **3** ($CDCl_3$), selected range.

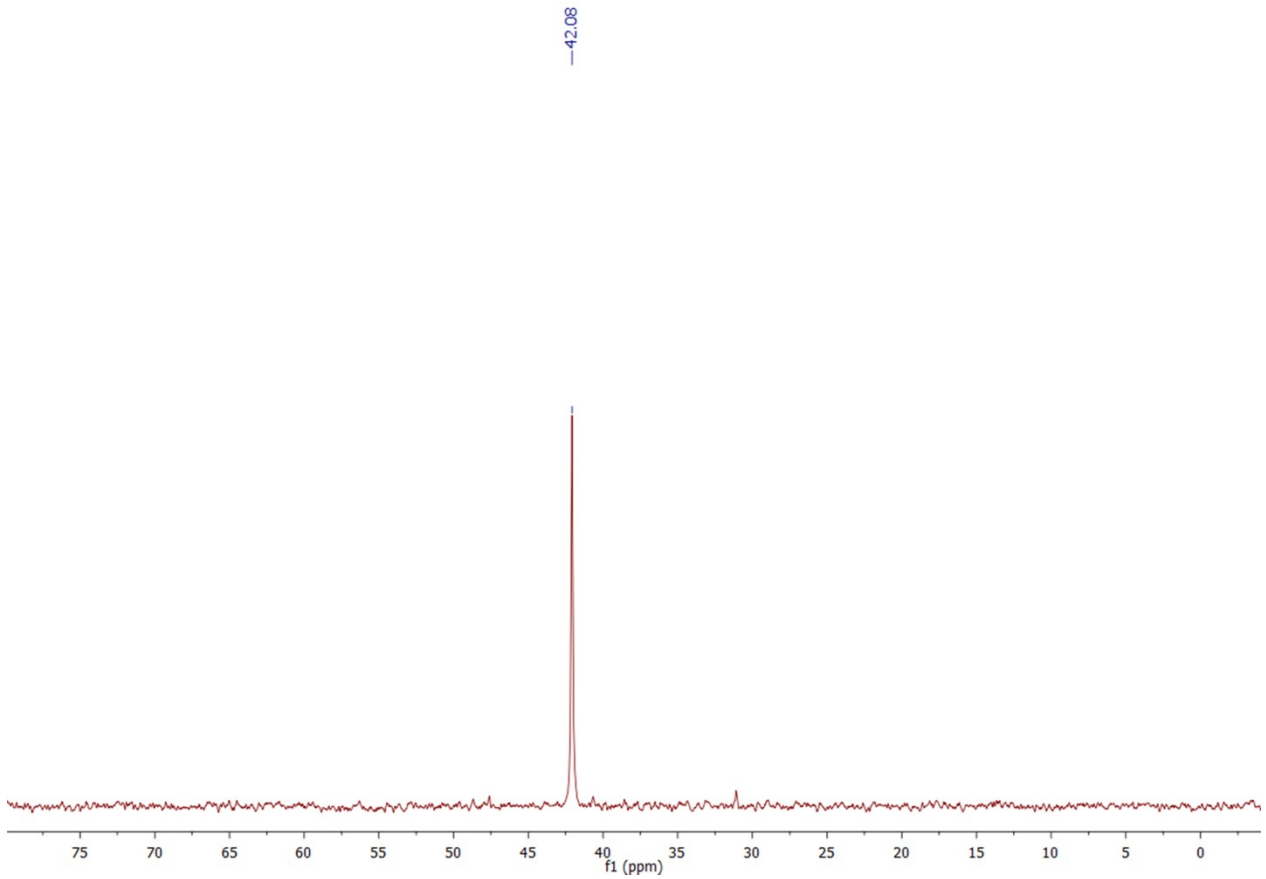

Figure S16. $^{31}P\{^{1}H\}$ NMR spectrum of **4** ($CDCl_3$), selected range.

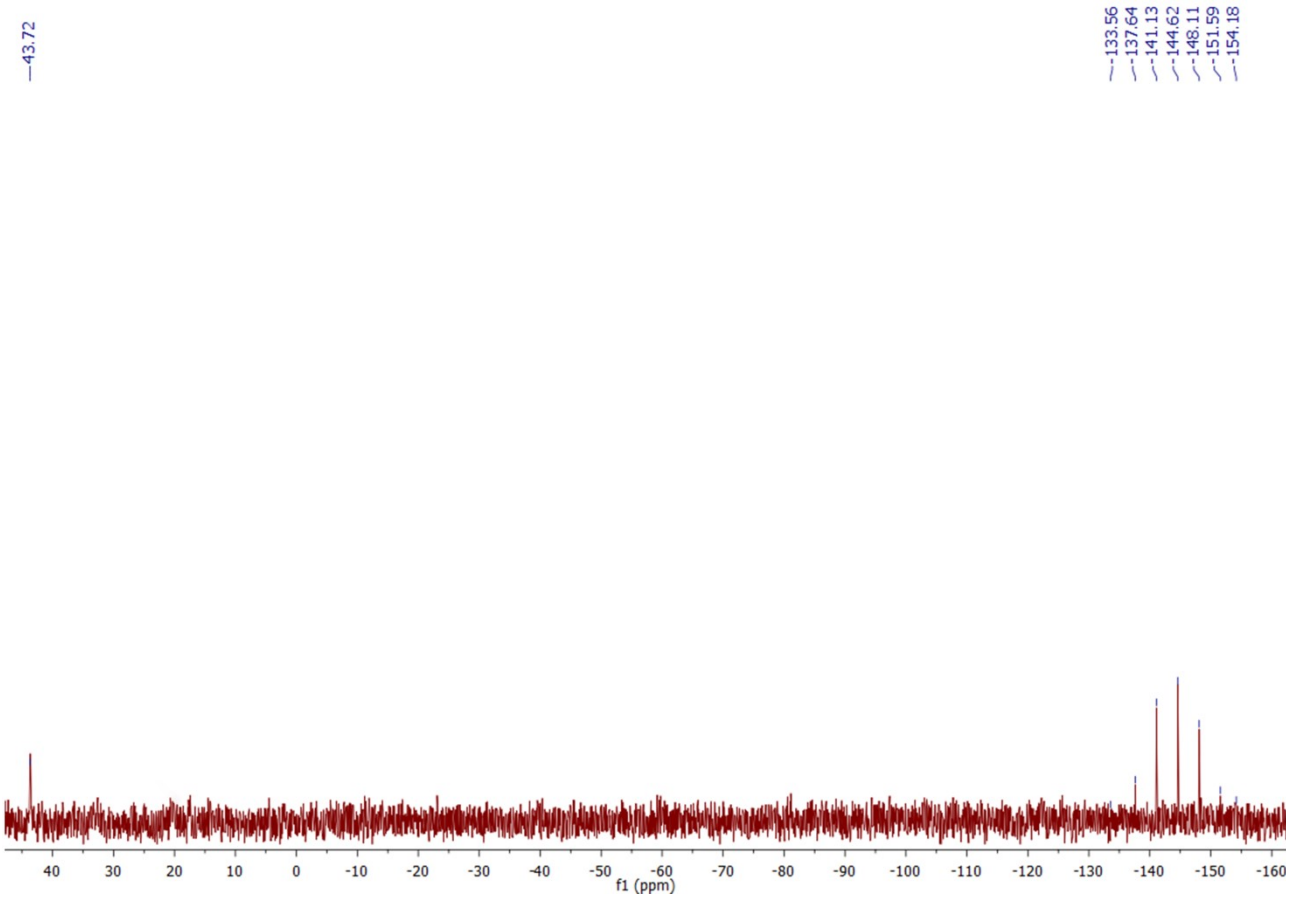

Figure S17. $^{31}P\{^{1}H\}$ NMR spectrum of **5** (CD_3CN), selected range.

§4. ESI-MS spectra

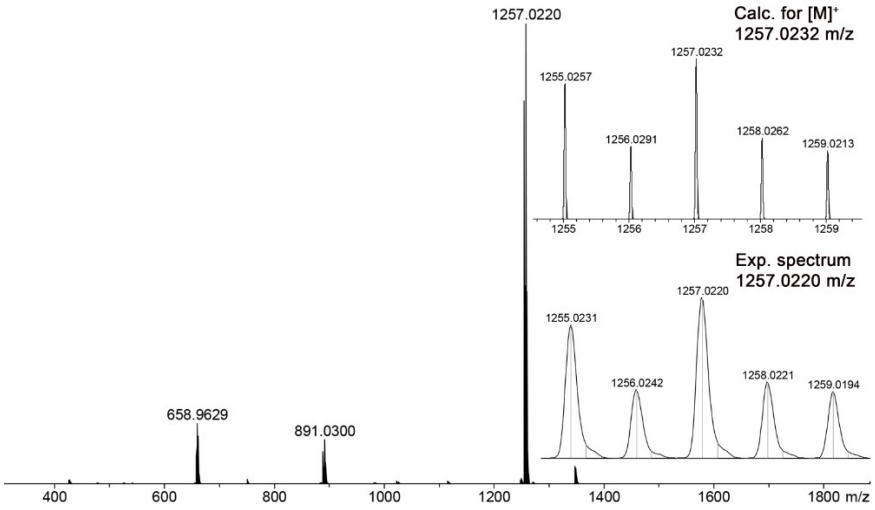

Figure S18. Experimental and calculated ESI^+ mass spectra of **2**.

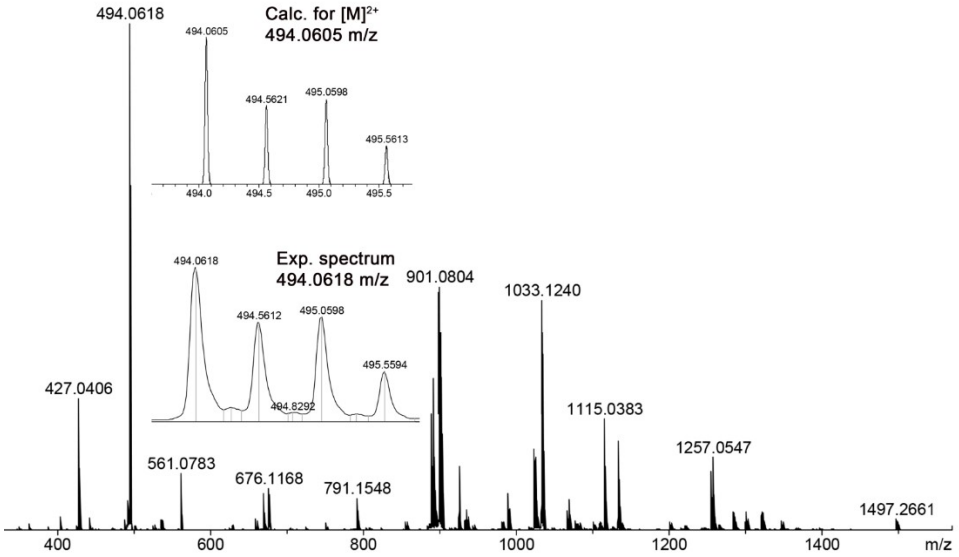

Figure S19. Experimental and calculated ESI$^+$ mass spectra of **3**.

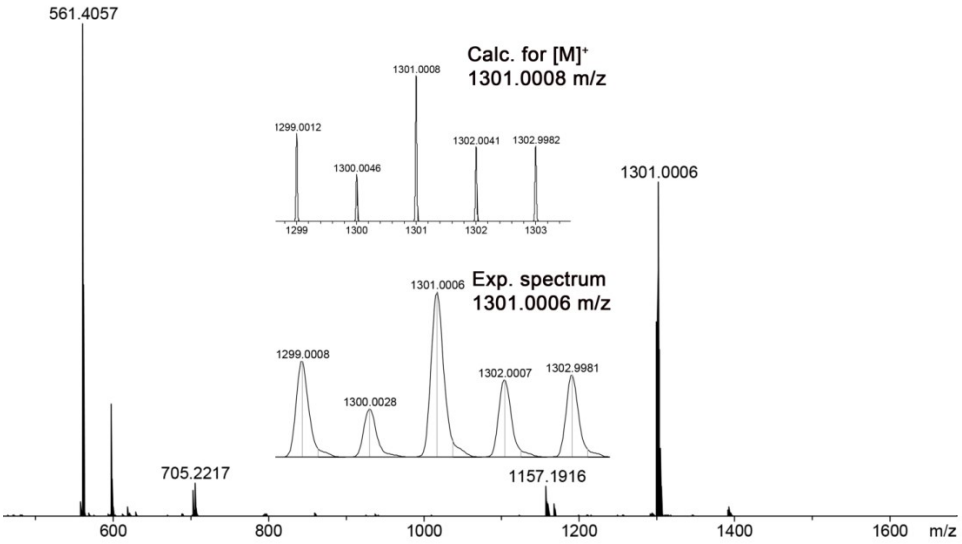

Figure S20. Experimental and calculated ESI$^+$ mass spectra of **4**.

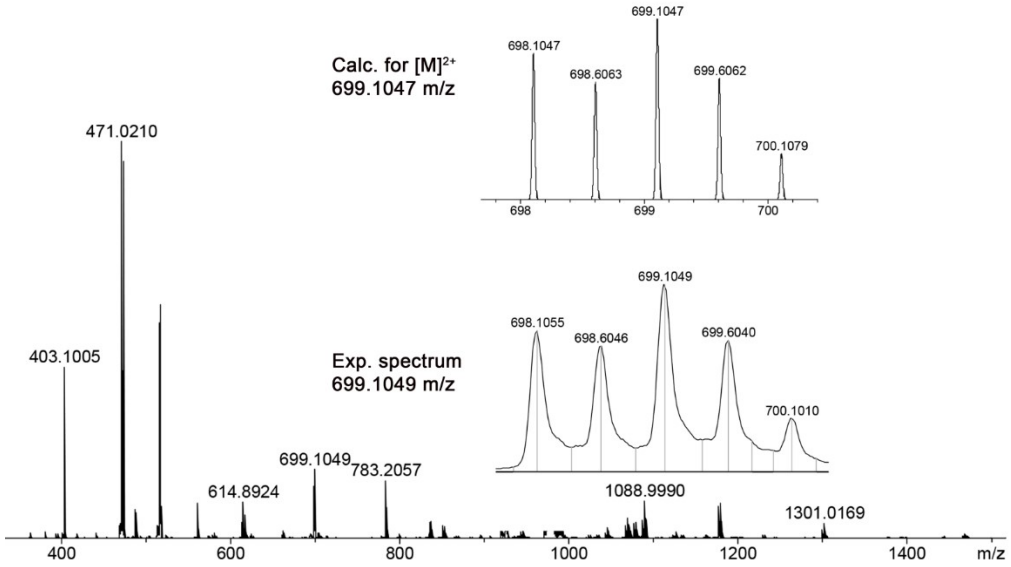

Figure S21. Experimental and calculated ESI$^+$ mass spectra of **5**.

§5. FT-IR spectra

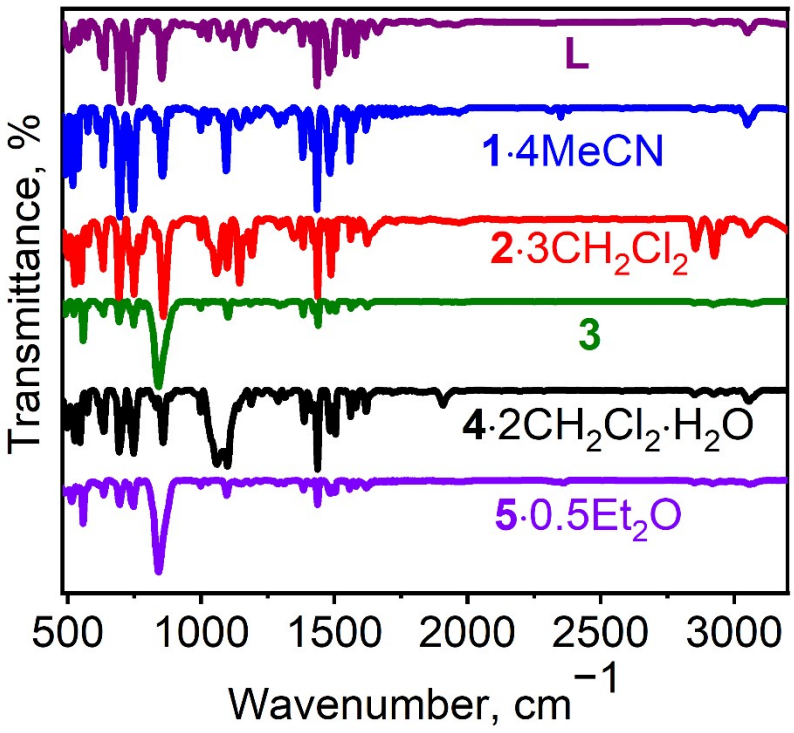

Figure S22. FT-IR spectra of **L** and complexes **1**–**5** (KBr).

§6. TGA&DTG curves

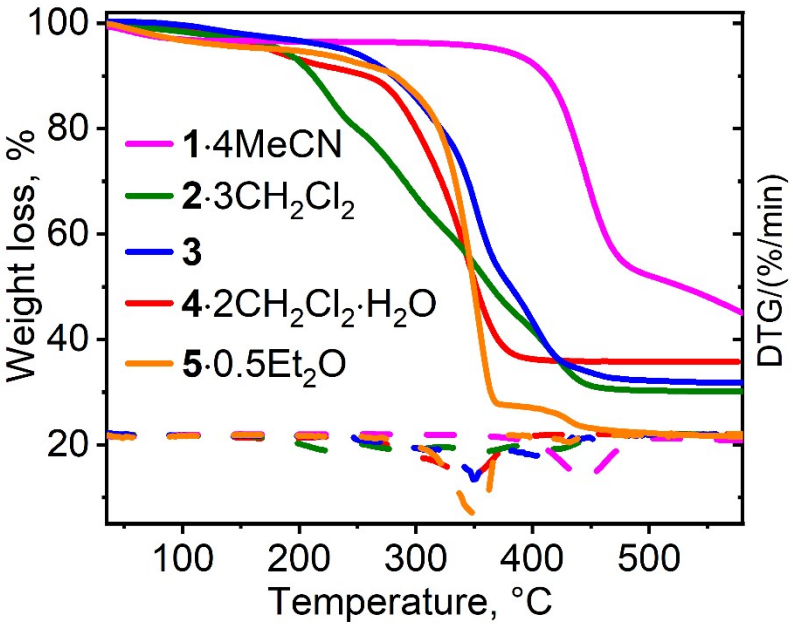

Figure S23. TGA (solid line) and DTG (dashed line) curves for complexes **1**–**5**.

§7. Details of DFT calculations

§7.1. Computational methodology

Starting molecular structural coordinates were obtained using the X-ray crystal structures of complexes **1-5**. The S_0 geometries of complexes **1**–**5** were optimized at the B3LYP-D4/ZORA-def2-TZVP (with segmented

all-electron relativistically contracted basis set SARC-ZORA-TZVP[5] for Ag, Au and I) level with relativistic corrections using the Zero-Order Regular Approximation (ZORA)[6,7] in a gas phase. The lowest triplet excited states (T_1) of cations **1–5** have been optimized at U-B3LYP-D4/ZORA-def2-TZVP level. To speed up the DFT calculations the SARC/J auxiliary basis set was applied for the RI-J approximation.

The method of quantum theory of atoms in molecules (QTAIM) was used to analyze the electronic structure of the studied complexes, more specifically the nature and energy of the metallophilic interactions M–M (M = Cu, Ag and Au). The QTAIM[8] topological descriptors at the bond critical points (BCPs) were calculated using the Multiwfn program (version 3.8)[9] and the results of all-electron calculations using the scalar relativistic the Zero-Order Regular Approximation (ZORA) and the B3LYP[10] functional with D4 dispersion correction.[11] These calculations were performed for the optimized geometries (B3LYP-D4/ZORA def2-TZVP, see above) of complexes **1**–**5** using the SARC-ZORA-TZVP for Ag, Au and I and the ZORA-def2-TZVP basis set for all other atoms.

Positions of the maxima and oscillator strengths of electronic transitions in the electronic absorption spectra (EAS) of complexes **1**–**5** were calculated using out all-electron TD-DFT calculations including spin-orbital coupling (SOC-TD-DFT) with the scalar relativistic the Zero-Order Regular Approximation (ZORA) and range-separated hybrid CAM-B3LYP functional[12] and SARC-ZORA-TZVP for Cu, Ag, Au and I and the ZORA-def2-TZVP basis sets[13,14] for all other atoms. The Tamm-Dankoff approximation (TDA)[15] was not used in these calculations. The solvent effect of CH_3CN was evaluated using the conductor-like solvation model CPCM.[16] The corresponding optimized geometries (B3LYP-D4 ZORA/def2-TZVP) of the complexes were used in the calculations related to the EAS and photophysical properties in solid state.

The ORCA 5.0.3 software package[14] was used for all calculations. MOs were visualized in Chemcraft.

§7.2. AIM analysis details

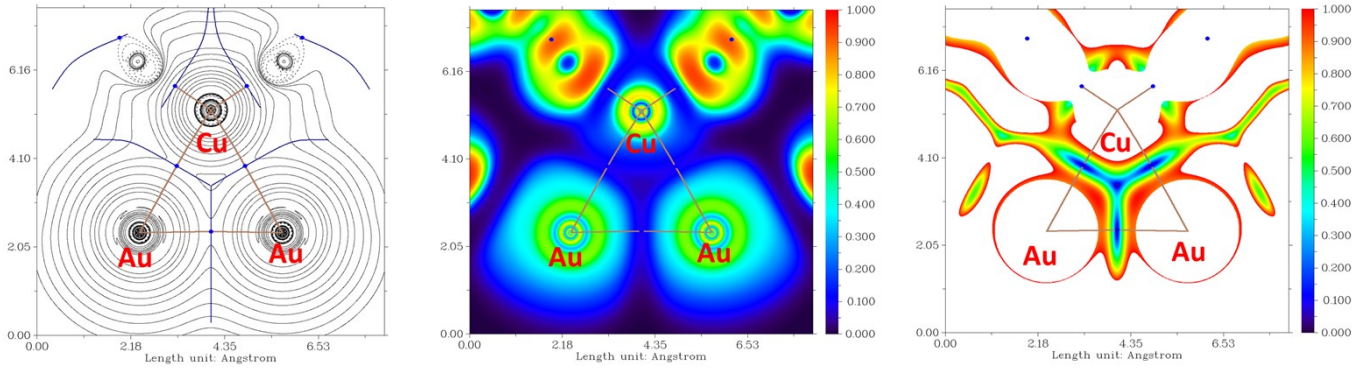

Figure S24. Contour line diagram of the Laplacian of electron density distribution $\nabla^2\rho(\mathbf{r})$, bond paths, and selected zero-flux surfaces (left), visualization of electron localization function (ELF, center) and reduced density gradient (RDG, right) analyses for metallophilic interactions **Au···Au** and **Cu···Au** in the $[Au_2CuL_2Cl_2]^+$ cation of **2**. Bond critical points (3, −1) are shown in blue, nuclear critical points (3, −3) – in pale brown, ring critical points (3, +1) – in orange, bond paths are shown as pale brown lines, length units – Å, and the color scale for the ELF and RDG maps are presented in a.u. (B3LYP-D4/ZORA-def2-TZVP).

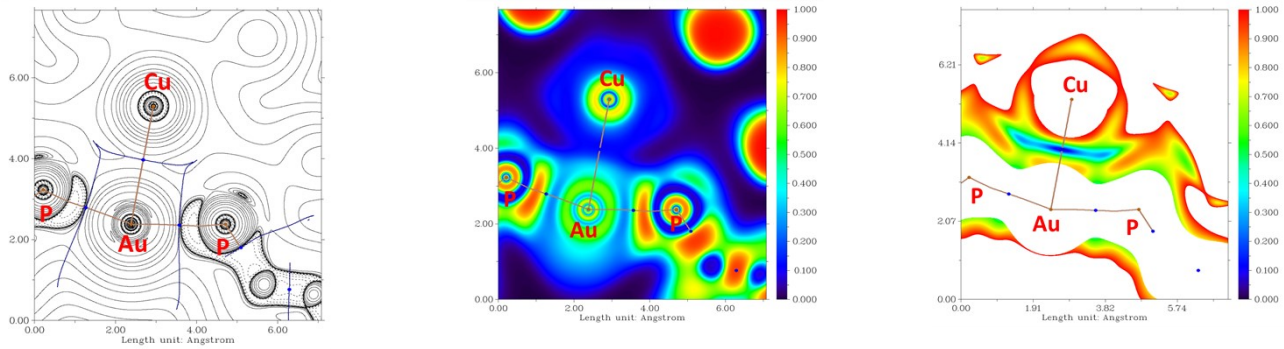

Figure S25. Contour line diagram of the Laplacian of electron density distribution $\nabla^2\rho(\mathbf{r})$, bond paths, and selected zero-flux surfaces (left), visualization of electron localization function (ELF, center) and reduced density gradient (RDG, right) analyses for metallophilic interactions and **Cu···Au** in the $[CuAuL_2]^{2+}$ cation of **3**. Bond critical points (3, −1) are shown in blue, nuclear critical points (3, −3) – in pale brown, ring critical points (3, +1) – in orange, bond paths are shown as pale brown lines, length units – Å, and the color scale for the ELF and RDG maps are presented in a.u. (B3LYP-D4/ZORA-def2-TZVP).

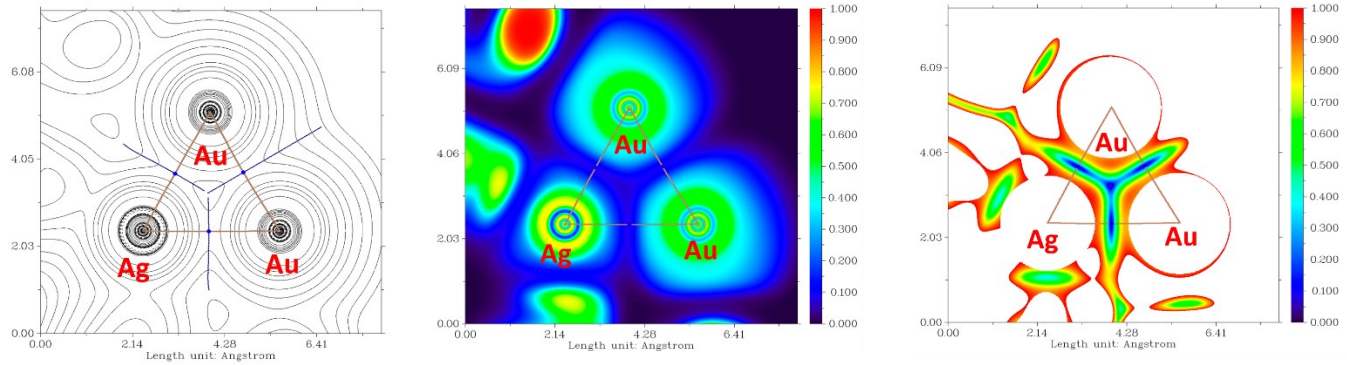

Figure S26. Contour line diagram of the Laplacian of electron density distribution $\nabla^2\rho(\mathbf{r})$, bond paths, and selected zero-flux surfaces (left), visualization of electron localization function (ELF, center) and reduced density gradient (RDG, right) analyses for metallophilic interactions **Au···Au** and **Ag···Au** in the $[Au_2AgL_2Cl_2]^+$ cation of **4**. Bond critical points (3, −1) are shown in blue, nuclear critical points (3, −3) – in pale brown, ring critical points (3, +1) – in orange, bond paths are shown as pale brown lines, length units – Å, and the color scale for the ELF and RDG maps are presented in a.u. (B3LYP-D4/ZORA-def2-TZVP).

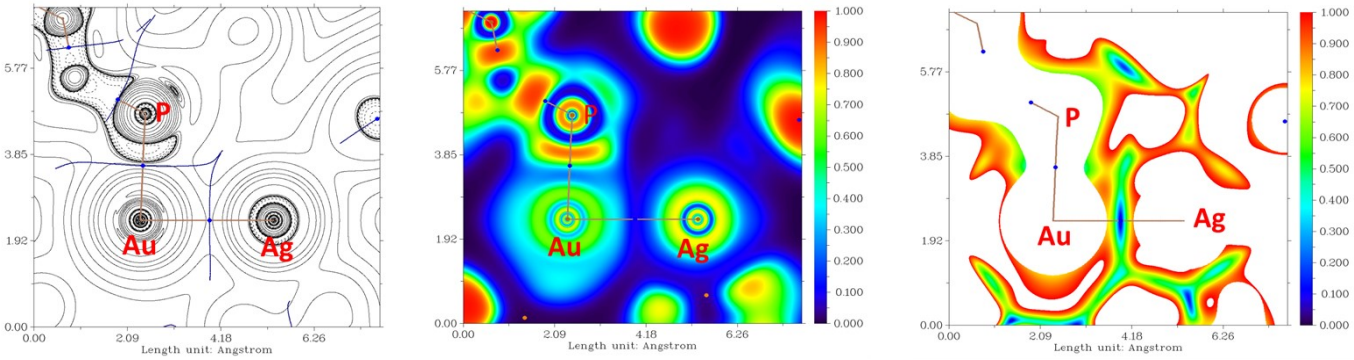

Figure S27. Contour line diagram of the Laplacian of electron density distribution $\nabla^2\rho(\mathbf{r})$, bond paths, and selected zero-flux surfaces (left), visualization of electron localization function (ELF, center) and reduced density gradient (RDG, right) analyses for metallophilic interactions **Ag···Au** in the $[AuAgL_3]^{2+}$ cation of **5**. Bond critical points (3, −1) are shown in blue, nuclear critical points (3, −3) – in pale brown, ring critical points (3, +1) – in orange, bond paths are shown as pale brown lines, length units – Å, and the color scale for the ELF and RDG maps are presented in a.u. (B3LYP-D4/ZORA-def2-TZVP).

§7.3. Frontier molecular orbitals

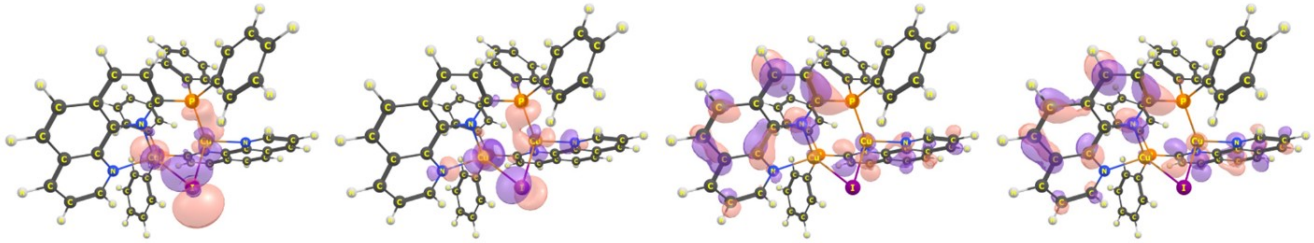

Figure S28. Selected frontier molecular orbitals (isovalue = 0.035) calculated for the optimized S_0 state geometry of $[Cu_2L_2(\mu_2\text{-}I)]^{2+}$ cation of **1** at CAM-B3LYP/ZORA-def2-TZVP//B3LYP-D4/ZORA-def2-TZVP level.

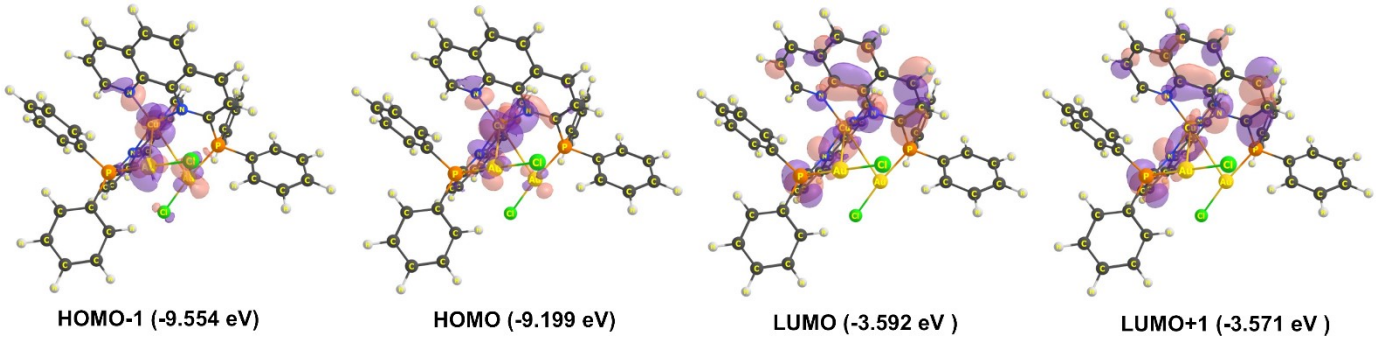

Figure S29. Selected frontier molecular orbitals (isovalue = 0.035) calculated for the optimized S_0 state geometry $[Au_2CuL_2Cl_2]^{+}$ cation of **2** at CAM-B3LYP/ZORA-def2-TZVP//B3LYP-D4/ZORA-def2-TZVP level.

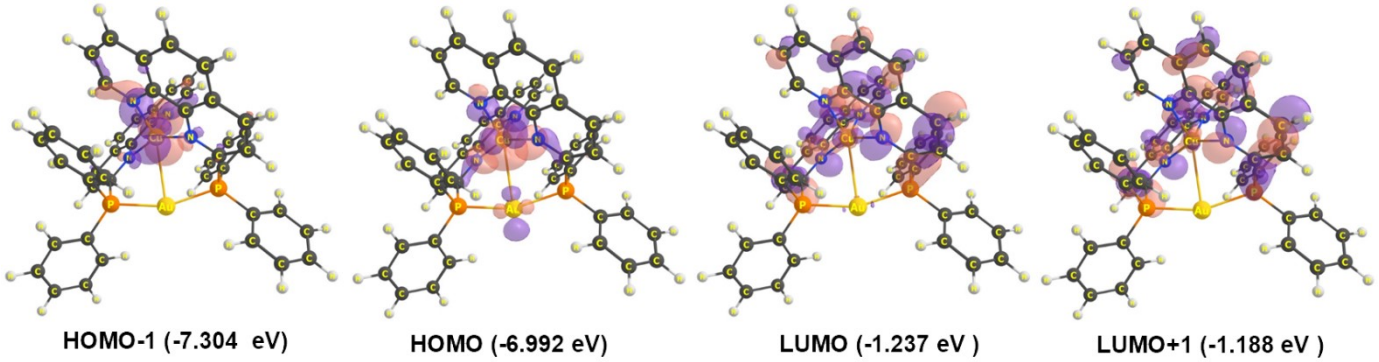

Figure S30. Selected frontier molecular orbitals (isovalue = 0.035) calculated for the optimized S_0 state geometry of $[CuAuL_2]^{2+}$ cation of **3** at CAM-B3LYP/ZORA-def2-TZVP//B3LYP-D4/ZORA-def2-TZVP level.

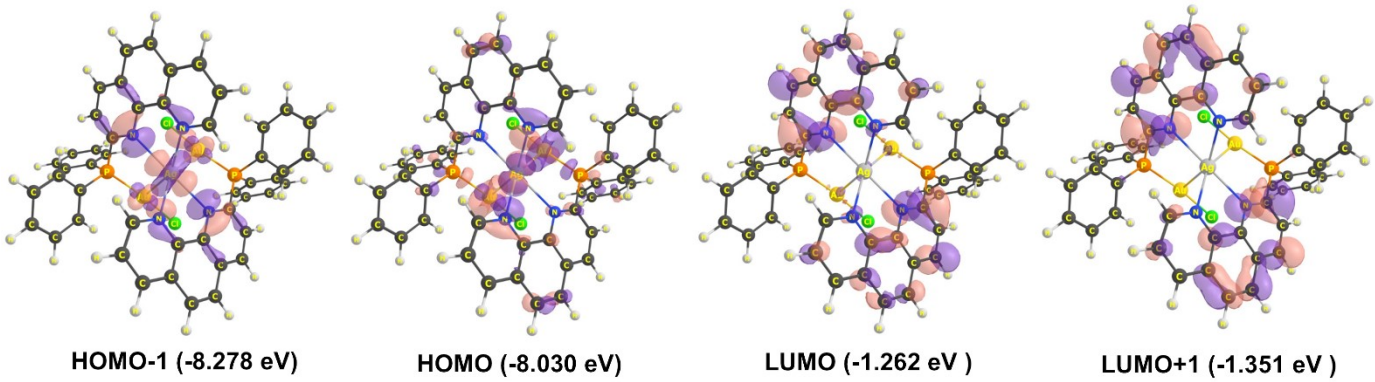

Figure S31. Selected frontier molecular orbitals (isovalue = 0.035) calculated for the optimized S_0 state geometry of $[Au_2AgL_2Cl_2]^+$ cation of **4** at CAM-B3LYP/ZORA-def2-TZVP//B3LYP-D4/ZORA-def2-TZVP.

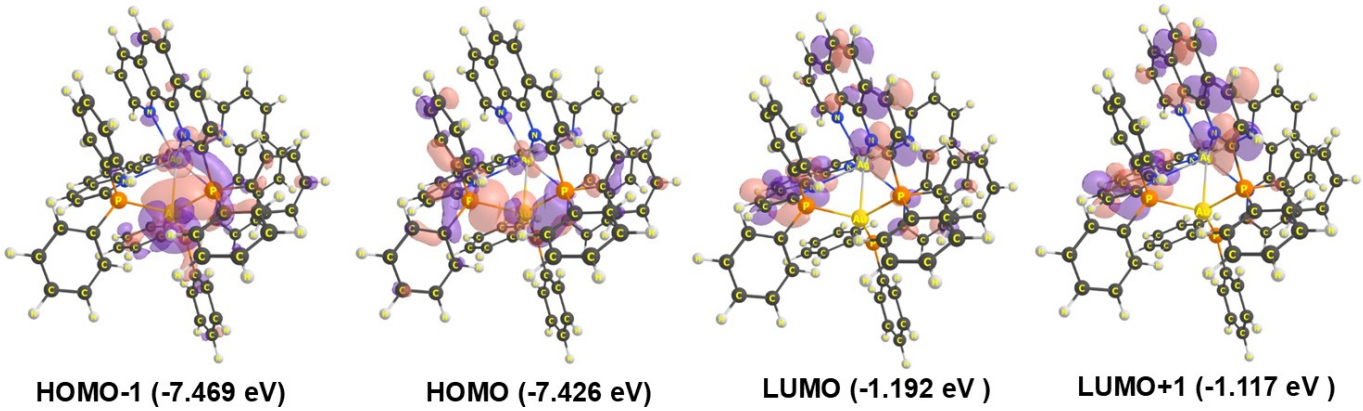

Figure S32. Selected frontier molecular orbitals (isovalue = 0.035) calculated for the optimized S_0 state geometry of $[AuAgL_3]^{2+}$ cation of **5** at CAM-B3LYP/ZORA-def2-TZVP//B3LYP-D4/ZORA-def2-TZVP level.

Table S2. Atomic contributions to selected molecular orbitals of cation $[Cu_2L_2(\mu_2\text{-}I)]^{2+}$ of **1** in the ground state (S_0) geometry according Hirshfeld population analysis at CAM-B3LYP/ZORA-def2-TZVP//B3LYP-D4/ZORA-def2-TZVP level.

MO	Energy, eV	Contribution, %		
		Cu	**I**	**2-(Ph_2P)Phen**
LUMO+10	0.42532	1.40	2.09	96.51
LUMO+9	0.26749	3.81	5.48	90.71
LUMO+8	0.18694	1.52	0.35	98.13
LUMO+7	0.14204	1.11	0.09	98.8
LUMO+6	-0.00490	2.23	1.22	96.55
LUMO+5	-0.05034	2.03	1.21	96.76
LUMO+4	-0.07946	4.64	0.38	94.98
LUMO+3	-1.09554	1.02	0.24	98.74
LUMO+2	-1.12003	1.45	0.64	97.91
LUMO+1	-1.18779	1.37	0.52	98.11
LUMO	-1.23704	1.76	0.52	97.72
HOMO	-6.99202	53.02	11.06	35.92
HOMO-1	-7.30414	42.14	30.56	27.3
HOMO-2	-7.35747	46.03	32.86	21.11
HOMO-3	-7.68483	38.17	40.94	20.89
HOMO-4	-8.03858	62.42	1.97	35.61

HOMO-5	-8.23477	25.44	23.31	51.25
HOMO-6	-8.24076	15.65	0.27	84.08
HOMO-7	-8.37247	13.80	6.15	80.05
HOMO-8	-8.42553	44.76	3.55	51.69
HOMO-9	-8.58308	34.19	4.68	61.13
HOMO-10	-8.61955	22.75	0.49	76.76
HOMO-11	-8.70200	0.99	0.22	98.79
HOMO-12	-8.72349	32.88	0.59	66.53

Table S3. Atomic contributions to selected molecular orbitals of $[Au_2CuL_2Cl_2]^+$ cation of **2** in the ground state (S_0) geometry according Hirshfeld population analysis at CAM-B3LYP/ZORA-def2-TZVP//B3LYP-D4/ZORA-def2-TZVP level.

MO	Energy, eV	Contribution, %			
		Cu	**Au**	**Cl**	**2-(Ph_2P)Phen**
LUMO+10	-1.861	0.45	5.92	1.38	92.25
LUMO+9	-1.99243	0.32	2.87	1.21	95.6
LUMO+8	-2.11761	1.68	9.02	3.22	86.08
LUMO+7	-2.21285	1.24	0.88	0.26	97.62
LUMO+6	-2.29475	1.03	10.51	2.29	86.17
LUMO+5	-2.347	0.83	2.61	0.40	96.16
LUMO+4	-2.45449	2.04	3.11	0.46	94.39
LUMO+3	-3.42594	1.02	1.17	0.47	97.34
LUMO+2	-3.43029	1.12	0.40	0.21	98.27
LUMO+1	-3.57098	2.07	1.15	0.56	96.22
LUMO	-3.59248	3.47	1.58	0.86	94.09
HOMO	-9.19861	64.98	5.50	1.03	28.49
HOMO-1	-9.55426	29.44	16.96	3.52	50.08
HOMO-2	-10.0174	22.39	27.57	19.53	30.51
HOMO-3	-10.24	28.81	9.58	17.66	43.95
HOMO-4	-10.3491	30.85	8.07	20.94	40.14
HOMO-5	-10.4147	2.41	14.60	30.56	52.43
HOMO-6	-10.4955	16.24	10.24	39.98	33.54
HOMO-7	-10.5521	6.68	10.99	38.15	44.18
HOMO-8	-10.5562	42.06	9.36	32.78	15.8
HOMO-9	-10.5687	25.20	8.67	29.51	36.62
HOMO-10	-10.6386	5.83	7.95	3.86	82.36
HOMO-11	-10.674	4.50	1.88	6.50	87.12
HOMO-12	-10.723	19.53	5.48	13.00	61.99

Table S4. Atomic contributions to selected molecular orbitals of $[CuAuL_2]^{2+}$ cation of **3** in the ground state (S_0) geometry according Hirshfeld population analysis at CAM-B3LYP/ZORA-def2-TZVP//B3LYP-D4/ZORA-def2-TZVP level.

MO	Energy, eV	Contribution. %		
		Au	**Cu**	**2-(Ph_2P)Phen**
LUMO+10	-4.20283	9.92	2.38	87.7
LUMO+9	-4.35386	12.99	1.96	85.05
LUMO+8	-4.56719	1.48	0.89	97.63
LUMO+7	-4.62815	15.36	0.54	84.1
LUMO+6	-4.65373	2.40	0.80	96.8

LUMO+5	-4.88203	12.91	0.76	86.33
LUMO+4	-5.08694	13.39	4.51	82.1
LUMO+3	-5.73484	2.14	1.08	96.78
LUMO+2	-5.76451	1.93	1.17	96.9
LUMO+1	-6.06846	1.67	3.22	95.11
LUMO	-6.08451	1.80	1.64	96.56
HOMO	-11.8087	6.61	64.63	28.76
HOMO-1	-12.1527	0.61	64.75	34.64
HOMO-2	-12.6099	9.53	27.71	62.76
HOMO-3	-12.7046	4.18	2.30	93.52
HOMO-4	-12.9516	1.20	26.96	71.84
HOMO-5	-12.9971	0.40	42.94	56.66
HOMO-6	-13.0964	0.53	53.59	45.88
HOMO-7	-13.1076	0.36	11.90	87.74
HOMO-8	-13.1122	0.11	0.15	99.74
HOMO-9	-13.2104	1.60	5.18	93.22
HOMO-10	-13.2393	0.68	57.95	41.37
HOMO-11	-13.3212	1.03	7.15	91.82
HOMO-12	-13.3677	1.46	17.97	80.57
LUMO+10	-4.20283	9.92	2.38	87.7

Table S5. Atomic contributions to selected molecular orbitals of $[Au_2AgL_2Cl_2]^+$ cation of **4** in the ground state (S_0) geometry according Hirshfeld population analysis at CAM-B3LYP/ZORA-def2-TZVP//B3LYP-D4/ZORA-def2-TZVP level.

MO	Energy, eV	Contribution, %			
		Au	**Ag**	**Cl**	**2-(Ph_2P)Phen**
LUMO+10	0.27212	6.33	2.51	1.29	89.87
LUMO+9	0.09061	4.64	0.64	1.92	92.8
LUMO+8	-0.01361	3.85	2.07	1.64	92.44
LUMO+7	-0.07728	3.53	0.51	1.34	94.62
LUMO+6	-0.15783	9.21	0.82	3.48	86.49
LUMO+5	-0.21497	4.47	1.38	0.64	93.51
LUMO+4	-0.60383	20.60	10.19	4.24	64.97
LUMO+3	-1.09091	0.56	1.01	0.21	98.22
LUMO+2	-1.09391	1.75	0.92	0.54	96.79
LUMO+1	-1.26153	1.32	0.81	0.55	97.32
LUMO	-1.35106	4.39	3.75	1.54	90.32
HOMO	-8.03042	24.84	18.47	2.56	54.13
HOMO-1	-8.14198	9.89	40.57	2.00	47.54
HOMO-2	-8.18144	1.96	3.63	1.31	93.1
HOMO-3	-8.27750	8.16	5.13	3.48	83.23
HOMO-4	-8.55723	3.27	1.00	1.55	94.18
HOMO-5	-8.59261	3.47	14.28	2.47	79.78
HOMO-6	-8.71370	4.02	4.89	3.55	87.54
HOMO-7	-8.76295	4.11	0.89	3.99	91.01
HOMO-8	-8.84758	2.38	0.15	3.32	94.15
HOMO-9	-8.85765	3.49	0.70	7.65	88.16
HOMO-10	-8.96296	2.64	0.58	4.84	91.94
HOMO-11	-8.96813	1.33	1.31	1.04	96.32
HOMO-12	-9.02391	5.01	0.41	7.73	86.85

Table S6. Atomic contributions to selected molecular orbitals of $[AuAgL_3]^{2+}$ cation of **5** in the ground state (S_0) geometry according Hirshfeld population analysis at CAM-B3LYP/ZORA-def2-TZVP//B3LYP-D4/ZORA-def2-TZVP level.

MO	Energy, eV	Contribution, %		
		Au	**Ag**	**2-(Ph_2P)Phen**
LUMO+10	0.09578	1.15	0.38	98.47
LUMO+9	-0.05197	0.87	0.24	98.89
LUMO+8	-0.05333	0.88	0.25	98.87
LUMO+7	-0.17905	3.02	0.29	96.69
LUMO+6	-0.56110	16.47	7.87	75.66
LUMO+5	-0.93281	0.92	0.78	98.3
LUMO+4	-1.00465	0.27	0.65	99.08
LUMO+3	-1.00601	0.27	0.65	99.08
LUMO+2	-1.11513	0.48	0.62	98.9
LUMO+1	-1.11731	0.48	0.62	98.9
LUMO	-1.12193	0.69	0.63	98.68
HOMO	-7.46224	20.20	6.30	73.5
HOMO-1	-7.46931	20.07	6.37	73.56
HOMO-2	-7.87939	2.52	41.84	55.64
HOMO-3	-7.88347	2.25	41.74	56.01
HOMO-4	-8.13926	1.72	2.70	95.58
HOMO-5	-8.18851	2.07	2.10	95.83
HOMO-6	-8.18988	2.05	2.14	95.81
HOMO-7	-8.42390	2.35	4.66	92.99
HOMO-8	-8.53274	0.22	0.49	99.29
HOMO-9	-8.53383	0.23	0.50	99.27
HOMO-10	-8.65628	7.29	8.02	84.69
HOMO-11	-8.77520	5.78	11.94	82.28
HOMO-12	-8.78880	0.38	0.12	99.5

Table S7. Metal···metal distances (Å) in **1–5**: the experimental data, and optimized S_0 and T_1 geometries.

		X-Ray derived values	B3LYP-D4/ZORA-def2-TZVP	
			Ground state (S_0)	Excited T_1 state
1	Cu3···Cu4	2.84	2.81	2.53
2	Au1···Au2	3.49	3.31	3.42
	Au1···Cu1	3.28	3.29	2.92
	Au2···Cu1	3.28	3.29	2.92
3	Au1···Cu1	2.87	2.97	2.74
4	Au1···Au2	3.31	3.22	3.37
	Au1···Ag1	3.10	3.17	3.02
	Au1···Ag2	3.31	3.17	2.84
5	Au1···Ag1	2.93	2.98	2.91

Table S8. Calculated $\Delta E(T_1–S_0)$ energy gaps for the S_0 and T_1 state structures of **1–5** optimized at B3LYP-D4//ZORA-def2-TZVP level.

	$\Delta E(T_1\text{-}S_0)$, eV / nm	$\lambda_{phos.}$, nm (eV)[a]
$[Cu_2L_2(\mu_2\text{-}I)]^{2+}$ **(1)**	1.665 / 745	715 (1.734)
$[Au_2CuL_2Cl_2]^{+}$ **(2)**	1.367 / 907	–
$[CuAuL_2]^{2+}$ **(3)**	1.761 / 704	720 (1.722)
$[Au_2AgL_2Cl_2]^{+}$ **(4)**	2.301 / 539	600 (2.066)
$[AuAgL_3]^{2+}$ **(5)**	2.206 / 562	605 (2.049)

[a] Band maxima in the phosphorescence spectra of **1** and **3**–**5** (**2** is non-emissive).

§7.4. Electronic absorption spectra: experimental and theoretical data

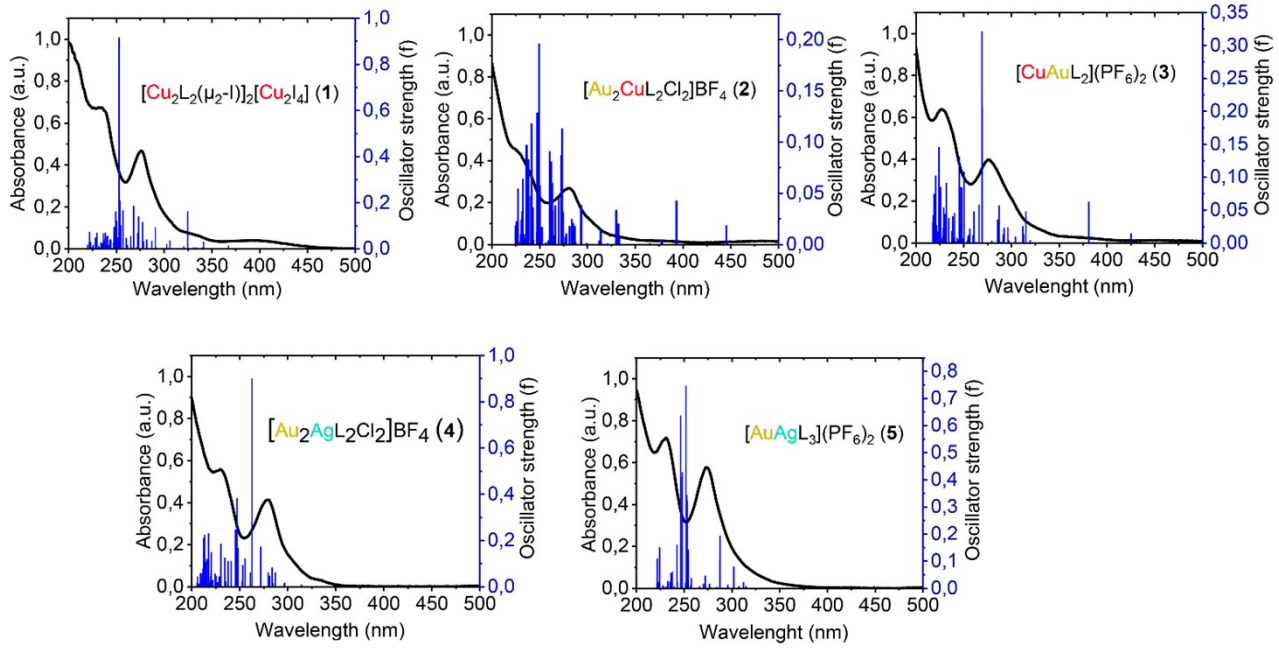

Figure S33. Experimental electronic absorption spectra (solid black curves) of **1**–**5** (MeCN, 298 K) and electronic transitions (vertical bars) calculated for the $[Cu_2L_2(\mu_2\text{-}I)]^{2+}$, $[Au_2CuL_2Cl_2]^{+}$, $[CuAuL_2]^{2+}$, $[Au_2AgL_2Cl_2]^{+}$ and $[AuAgL_3]^{2+}$ cations, respectively **5** calculated at CAM-B3LYP/def2-TZVP//B3LYP-D4/ZORA-def2-TZVP level.

Table S9. Calculated (energies and characters of the main singlet excitations ($f > 0.01$) of $[Cu_2L_2(\mu_2\text{-}I)]^{2+}$ cation of **1**.

state	E, eV	λ, nm	*f*	Transitions (main contributions)	Character
7	3.818	324.7	0.163	HOMO -> LUMO+1 (56%) HOMO-2 -> LUMO+3 (12%) HOMO-2 -> LUMO+2 (10%)	(CuI)LCT
19	4.471	277.3	0.119	HOMO-8 -> LUMO+1 (9%) HOMO-7 -> LUMO+2 (12%) HOMO-6 -> LUMO+4 (10%) HOMO-3 -> LUMO+3 (8%) HOMO-1 -> LUMO+4 (10%)	(CuI)LCT + (L)LCT
20	4.538	273.2	0.142	HOMO-4 -> LUMO+1 (22%) HOMO-3 -> LUMO+3(25%)	(CuI)LCT + (L)LCT
24	4.626	268	0.182	HOMO-8 -> LUMO+1 (14%) HOMO-4 -> LUMO+1 (14%) HOMO-3 -> LUMO+2 (11%)	(CuI)LCT + (L)LCT

31	4.828	256.8	0.167	HOMO-2 -> LUMO+5 (34%) HOMO-2 -> LUMO+20 (7%) HOMO -> LUMO+10 (8%)	(CuI)LCT + (L)LCT
33	4.889	253.6	0.210	HOMO-8 -> LUMO+1 (7%) HOMO-3 -> LUMO+3 (10%) HOMO -> LUMO+10 (16%)	(CuI)LCT + (L)LCT
35	4.902	252.9	0.913	HOMO-10 -> LUMO+1 (26%) HOMO-8 -> LUMO+1 (12%)	(CuI)LCT + (L)LCT
37	4.951	250.4	0.118	HOMO-2 -> LUMO+6 (11%) HOMO-1 -> LUMO+7 (9%) HOMO -> LUMO+10 (21%)	(CuI)LCT + (L)LCT
38	4.975	249.2	0.161	HOMO-9 -> LUMO+2 (7%) HOMO-4 -> LUMO+4 (21%) HOMO-3 -> LUMO+3 (7%) HOMO -> LUMO+10 (7%)	(CuI)LCT + (L)LCT

Table S10. Calculated energies and characters of the main singlet excitations ($f > 0.01$) of $[Au_2CuL_2Cl_2]^+$ cation of **2**.

state	E, eV	λ, nm	*f*	Transitions (main contributions)	Character
1	2.822	445.3	0.018	HOMO-1 -> LUMO (5%) HOMO -> LUMO+1 (7%) HOMO -> LUMO+2 (13%)	(Au+Cu)LCT+ (L)LCT
3	3.278875	393.1	0.042321	HOMO-2 -> LUMO (5%) HOMO-1 -> LUMO (7%) HOMO -> LUMO+1 (10%)	(Au+Cu+Cl)LCT+ (L)LCT
9	3.862	330.1	0.033	HOMO-6 -> LUMO (10%) HOMO-4 -> LUMO (31%) HOMO-2 -> LUMO (27%)	(Au+Cu+Cl)LCT+ (L)LCT
3	3.279	393.1	0.042	HOMO-3 -> LUMO+1 (5%) HOMO-3 -> LUMO+2 (8%)	(Au+Cu+Cl)LCT+ (L)LCT
15	4.232	293.3	0.038	HOMO-14 -> LUMO+1 (16%) HOMO-14 -> LUMO+2 (7%) HOMO-4 -> LUMO (7%) HOMO-2 -> LUMO (10%)	(Au+Cu+Cl)LCT+ (L)LCT
26	4.549	273.5	0.112	HOMO-7 -> LUMO (14%) HOMO-3 -> LUMO+1 (9%) HOMO-3 -> LUMO+2 (14%)	(Au+Cu+Cl)LCT+ (L)LCT
9	3.862	330.1	0.033	HOMO-12 -> LUMO+2 (11%) HOMO-6 -> LUMO+3 (9%) HOMO-5 -> LUMO+1 (11%)	(Au+Cu+Cl)LCT+ (L)LCT
49	5.154	241.4	0.118	HOMO-1 -> LUMO+5 (55%)	(Au+Cu)LCT+ (L)LCT
54	5.252	236.2	0.097	HOMO-2 -> LUMO+6 (18%) HOMO -> LUMO+9 (20%)	(Au+Cu)LCT+ (L)LCT

Table S11. Calculated energies and characters of the main singlet excitations ($f > 0.01$) of $[CuAuL_2]^{2+}$ cation of **3**.

state	E, eV	λ, nm	*f*	Transitions (main contributions)	Character
1	2.916	425.1	0.014	HOMO-1 -> LUMO+1 (10%)	(Au+Cu)LCT+ (L)LCT

				HOMO -> LUMO (74%)	
3	3.255	380.9	0.062	HOMO-1 -> LUMO+1 (72%) HOMO -> LUMO (13%)	(Au+Cu)LCT+ (L)LCT
10	3.937	315	0.047	HOMO-2 -> LUMO (39%) HOMO-1 -> LUMO+3 (22%)	(Au+Cu)LCT+ (L)LCT
11	3.962	312.9	0.013	HOMO-6 -> LUMO+1 (39%) HOMO-4 -> LUMO+1 (30%)	(Cu)LCT+ (L)LCT
12	3.974	312	0.025	HOMO-5 -> LUMO+1 (31%) HOMO -> LUMO+4 (30%)	(Au+Cu)LCT+ (L)LCT
13	4.076	304.2	0.010	HOMO-6 -> LUMO (24%) HOMO-4 -> LUMO (13%) HOMO -> LUMO+4 (14%)	(Au+Cu)LCT+(L)LCT
19	4.320	287	0.057	HOMO-10 -> LUMO (14%) HOMO-2 -> LUMO+2 (27%) HOMO -> LUMO+5 (12%)	(Au+Cu)LCT+(L)LCT
20	4.342	285.6	0.035	HOMO-3 -> LUMO+2 (15%) HOMO-2 -> LUMO+3 (26%)	(Au+Cu)LCT+(L)LCT
22	4.603	269.3	0.205	HOMO-3 -> LUMO+1 (14%) HOMO-2 -> LUMO+2 (18%)	(Au+Cu)LCT+(L)LCT
23	4.608	269	0.321	HOMO-6 -> LUMO+2 (10%) HOMO-3 -> LUMO (21%) HOMO-2 -> LUMO+3 (10%)	(Au+Cu)LCT+(L)LCT
34	4.953	250.3	0.108	HOMO-11 -> LUMO (10%) HOMO-9 -> LUMO+1 (10%)	(Au+Cu)LCT+(L)LCT
39	5.057	245.2	0.131	HOMO-11 -> LUMO+1 (10%) HOMO-6 -> LUMO+4 (22%) HOMO-4 -> LUMO+4 (16%)	(Au+Cu)LCT+(L)LCT
65	5.530	224.2	0.145	HOMO-3 -> LUMO+3 (12%) HOMO-2 -> LUMO+5 (10%)	(Au+Cu)LCT+(L)LCT

Table S12. Calculated energies and characters of the main singlet excitations ($f > 0.01$) of $[Au_2AgL_2Cl_2]^+$ cation of **4**.

state	E, eV	λ, nm	*f*	Transitions (main contributions)	Character
1	3.945	314.3	0.007	HOMO-1 -> LUMO (72%)	(Au+Ag+Cl)LCT + (L)LCT
4	4.185	296.3	0.013	HOMO-3 -> LUMO+1 (11%) HOMO-3 -> LUMO+3 (11%) HOMO-2 -> LUMO (36%)	(Au+Ag+Cl)LCT + (L)LCT
5	4.321	286.9	0.060	HOMO-3 -> LUMO (10%) HOMO-1 -> LUMO+1 (27%) HOMO -> LUMO (16%)	(Au+Ag+Cl)LCT + (L)LCT
10	4.561	271.9	0.171	HOMO-1 -> LUMO+2 (9%) HOMO-1 -> LUMO+4 (22%) HOMO -> LUMO+1 (37%)	(Au+Ag+Cl)LCT + (L)LCT
11	4.718	262.8	0.276	HOMO-5 -> LUMO+1 (13%) HOMO-4 -> LUMO (20%)	(Au+Ag+Cl)LCT + (L)LCT
12	4.718	262.8	0.899	HOMO-5 -> LUMO (20%) HOMO-4 -> LUMO+1 (11%) HOMO-4 -> LUMO+3 (8%)	(Au+Ag+Cl)LCT + (L)LCT
14	4.854	255.4	0.122	HOMO-5 -> LUMO (11%) HOMO-3 -> LUMO+4 (7%) HOMO -> LUMO (8%)	(Au+Ag+Cl)LCT + (L)LCT
17	4.997	248.1	0.166	HOMO-4 -> LUMO+2 (10%)	(Au+Ag+Cl)LCT + (L)LCT

				HOMO-2 -> LUMO (10%) HOMO-2 -> LUMO+2 (10%)	
18	5.020	247.0	0.382	HOMO-5 -> LUMO+2 (17%) HOMO-4 -> LUMO+3 (12%) HOMO-1 -> LUMO+3 (8%)	(Au+Ag+Cl)LCT + (L)LCT
19	5.053	245.4	0.246	HOMO-14 -> LUMO (6%) HOMO-6 -> LUMO (25%) HOMO-5 -> LUMO (6%) HOMO-5 -> LUMO+4 (9%)	(Au+Ag+Cl)LCT + (L)LCT
25	5.291	234.3	0.124	HOMO-15 -> LUMO (11%) HOMO -> LUMO+6 (8%)	(Au+Ag+Cl)LCT + (L)LCT
27	5.379	230.5	0.185	HOMO-7 -> LUMO+4 (5%) HOMO -> LUMO+5 (9%)	(Au+Ag+Cl)LCT + (L)LCT
28	5.381	230.4	0.077	HOMO-16 -> LUMO (20%) HOMO-16 -> LUMO+4 (9%) HOMO-14 -> LUMO (9%)	(Au+Ag+Cl)LCT + (L)LCT
44	5.706	217.3	0.230	HOMO-15 -> LUMO+1 (6%) HOMO-11 -> LUMO (7%) HOMO-8 -> LUMO+1 (6%) HOMO-6 -> LUMO+2 (5%) HOMO-3 -> LUMO+8 (5%)	(Au+Ag+Cl)LCT + (L)LCT
53	5.807	213.5	0.224	HOMO-15 -> LUMO+1 (5%) HOMO-1 -> LUMO+5 (5%)	(Au+Ag+Cl)LCT + (L)LCT

Table S13. Calculated energies and characters of the main singlet excitations ($f > 0.01$) of $[AuAgL_3]^{2+}$ cation of **5**.

State	E, eV	λ, nm	*f*	Transitions (main contributions)	Character
1	3.942	314.5	0.007	HOMO-2 -> LUMO (11%) HOMO-2 -> LUMO+5 (5%) HOMO-1 -> LUMO+2 (5%) HOMO -> LUMO (21%) HOMO -> LUMO+6 (9%)	(Au+Ag)LCT+ (L)LCT
3	3.972	312.2	0.021	HOMO-3 -> LUMO+1 (12%) HOMO-3 -> LUMO+3 (10%) HOMO-2 -> LUMO+2 (11%) HOMO-2 -> LUMO+4 (10%) HOMO-1 -> LUMO+1 (7%) HOMO-1 -> LUMO+2 (6%) HOMO -> LUMO+1 (5%) HOMO -> LUMO+2 (6%)	(Au+Ag)LCT+ (L)LCT
8	4.110	301.6	0.011	HOMO-4 -> LUMO+2 (8%) HOMO-2 -> LUMO+5 (9%) HOMO-1 -> LUMO (8%) HOMO-1 -> LUMO+1 (8%) HOMO-1 -> LUMO+6 (11%)	(Au+Ag)LCT+ (L)LCT
12	4.311	287.6	0.193	HOMO-6 -> LUMO+3 (12%) HOMO-5 -> LUMO+4 (5%) HOMO-4 -> LUMO+5 (9%) HOMO-1 -> LUMO+4 (7%) HOMO -> LUMO+1 (5%) HOMO -> LUMO+3 (17%)	(Au+Ag)LCT+ (L)LCT
13	4.314	287.4	0.105	HOMO-6 -> LUMO+5 (8%)	(Au+Ag)LCT(L)LCT

				HOMO-5 -> LUMO+4 (5%) HOMO-4 -> LUMO+3 (12%) HOMO-1 -> LUMO+4 (9%) HOMO -> LUMO+5 (6%)	
21	4.558	272	0.043	HOMO-3 -> LUMO+4 (5%) HOMO-2 -> LUMO+1 (5%) HOMO-2 -> LUMO+3 (10%) HOMO-2 -> LUMO+6 (7% HOMO-1 -> LUMO (7%) HOMO-1 -> LUMO+1 (7%) HOMO -> LUMO+2 (6%) HOMO -> LUMO+3 (5%)	(Au+Ag)LCT+(L)LCT
22	4.559	272	0.040	HOMO-3 -> LUMO+6 (17%) HOMO-1 -> LUMO (5%) HOMO -> LUMO (7%) HOMO -> LUMO+2 (9%)	(Au+Ag)LCT+(L)LCT
33	4.901	253	0.323	HOMO-7 -> LUMO+3 (7%) HOMO-6 -> LUMO (5%) HOMO-1 -> LUMO+3 (5%) HOMO -> LUMO+7 (6%)	(Au+Ag)LCT+(L)LCT
34	4.902	252.9	0.343	HOMO-8 -> LUMO (5%) HOMO-7 -> LUMO+4 (7%) HOMO-1 -> LUMO+4 (5%) HOMO-1 -> LUMO+7 (5%)	(Au+Ag)LCT+(L)LCT
35	4.922	251.9	0.746	HOMO-6 -> LUMO+3 (6%) HOMO-5 -> LUMO+4 (6%) HOMO-4 -> LUMO (7%)	(Au+Ag)LCT + (L)LCT
38	5.002	247.9	0.427	HOMO-7 -> LUMO+3 (3%) HOMO -> LUMO+5 (3%) HOMO -> LUMO+7 (43%) HOMO -> LUMO+12 (3%)	(Au+Ag)LCT + (L)LCT
40	5.036	246.2	0.635	HOMO-16 -> LUMO+6 (5%) HOMO-11 -> LUMO+6 (6%) HOMO-10 -> LUMO+6 (10%) HOMO-7 -> LUMO+6 (5%) HOMO-4 -> LUMO+6 (5%)	(Au+Ag)LCT + (L)LCT
66	5.532	224.1	0.146	HOMO-7 -> LUMO+3 (5%) HOMO-6 -> LUMO+6 (7%) HOMO-4 -> LUMO+3 (14%) HOMO -> LUMO+12 (8%)	(Au+Ag)LCT + (L)LCT
67	5.533	224.1	0.149	HOMO-7 -> LUMO+4 (5%) HOMO-5 -> LUMO+6 (7%) HOMO-4 -> LUMO+4 (14%)	(Au+Ag)LCT + (L)LCT

§8. Details of cytotoxic activity study

Cytotoxic activity study of the ligand **L** and clusters **1**–**5** was performed on hepatocellular carcinoma HepG2, laryngeal carcinoma Hep2, lung carcinoma A549 and non-tumor lung fibroblasts MRC5 human cell lines. All

cell lines except A549 cell line (BioloT Ltd., Russia) were purchased from the State Research Center of Virology and Biotechnology VECTOR (Novosibirsk, Russia). Cell viability was assessed by double staining with fluorescent dyes Hoechst 33342/propidium iodide (PI) according to the standard method.[17]

Cells were seeded on a 96-well plate (Jet Biofil, TCP011096) with a seeding cells density of 2×10^4/cm^2 and cultured in medium (DMEM for HepG2, Hep2 and MRC5 cells and DMEM/F12 for A549 cells) containing 10% fetal bovine serum (FBS, HyClone) and GlutaMAX supplement (Gibco, 35050061) for 24 h under standard conditions (humidified atmosphere, 5% CO_2, 37 °C). Ligand **L** (1–32 μM in DMSO) and tested complexes **1–5** (0.5–16 μM in DMSO) were then added and incubated for 24 h, the final concentration of DMSO < 1% (v/v). After incubation, cells were stained with a mixture of Hoechst 33342 (Sigma-Aldrich) and PI (Invitrogen) fluorescent dyes for 30 min at 37 °C. Images were then acquired (4 fields per well, 200× magnification) using an IN Cell Analyzer 2200 imaging system (GEHealthcare, UK) and analyzed using IN Cell Investigator software (version 1.5, GEHealthcare, UK) to identify dead, live and apoptotic cells in the whole population. Cytotoxic activity was assessed using the IC_{50} parameters calculated from cell survival (%) versus drug concentration (μM) plots. Selectivity indices (SI) were determined as the ratio of the IC50 on the MRC5 line to its values on tumor cell lines. All data presented are the mean of three wells. Quantitative data are expressed as mean ± standard deviation (SD).

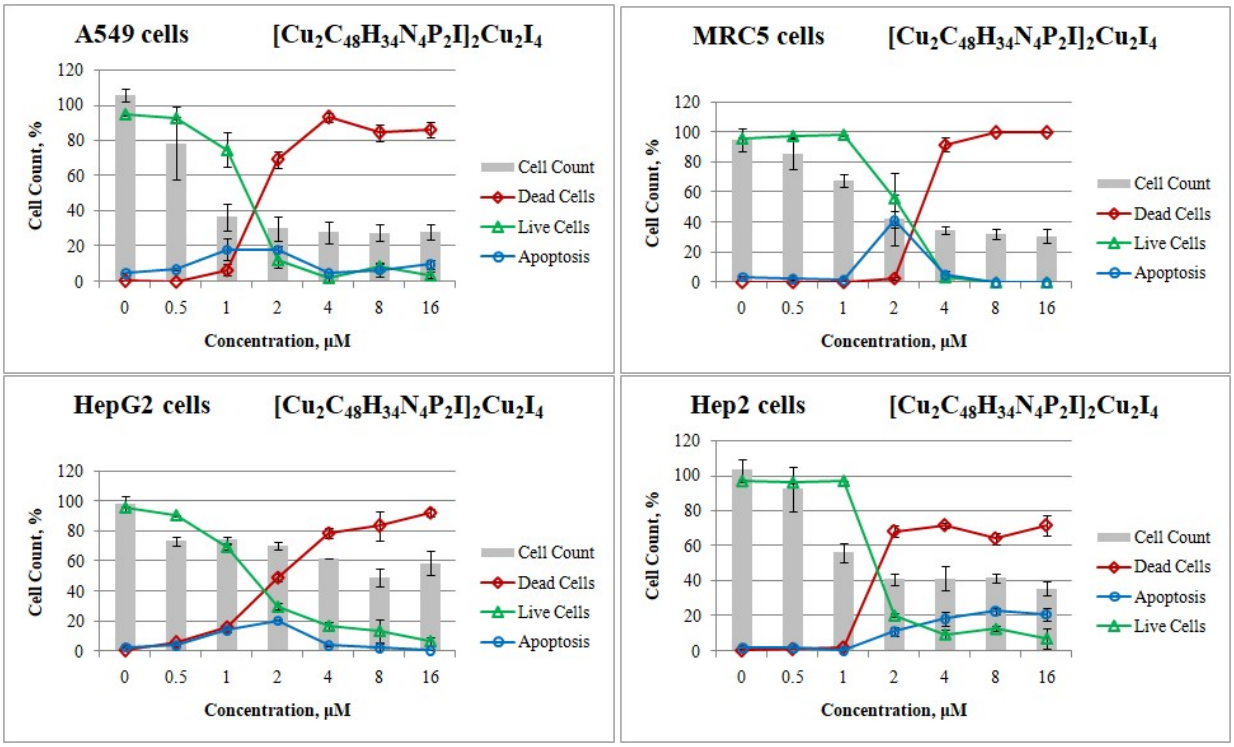

Figure S34. The effect of **1** on the viability of A549, MRC5, HepG2 and Hep2 cells determined after 24 h by Hoechst 33342/propidium iodide staining.

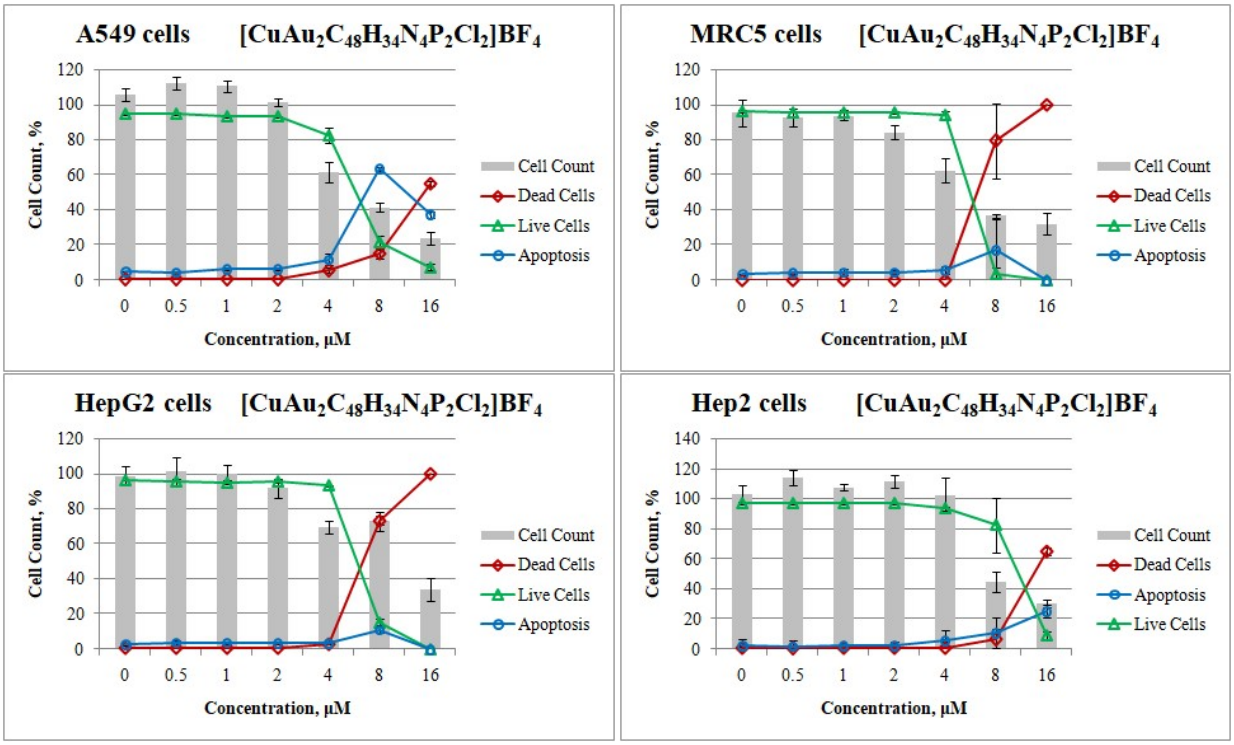

Figure S35. The effect of complex **2** on the viability of A549, MRC5, HepG2 and Hep2 cells determined after 24 h by Hoechst 33342/propidium iodide staining.

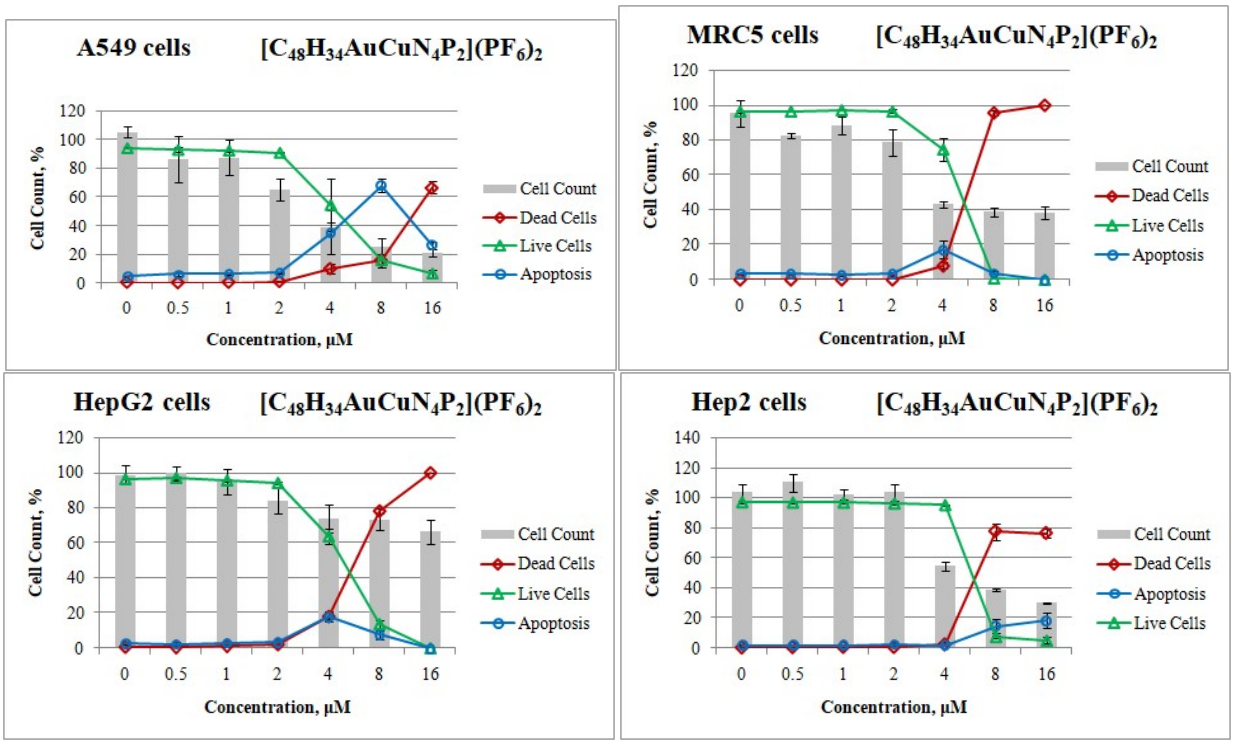

Figure S36. The effect of complex **3** on the viability of A549, MRC5, HepG2 and Hep2 cells determined after 24 h by Hoechst 33342/propidium iodide staining.

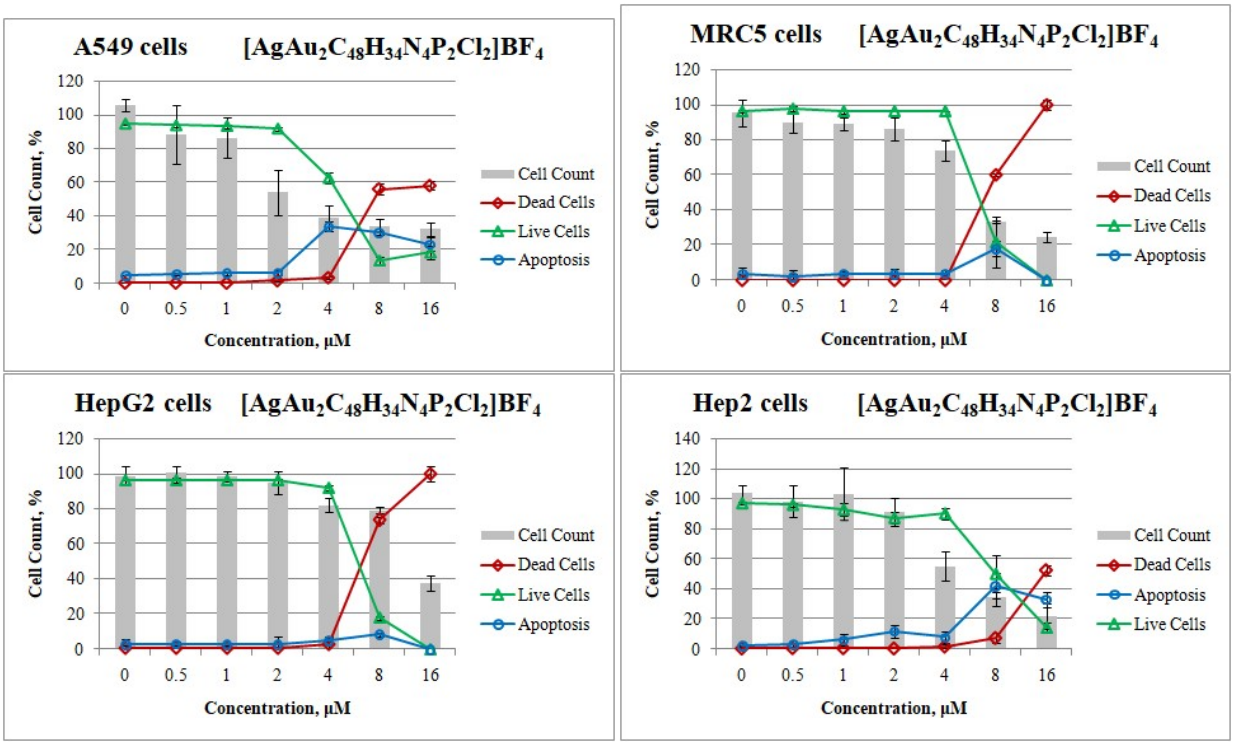

Figure S37. The effect of complex **4** on the viability of A549, MRC5, HepG2 and Hep2 cells determined after 24 h by Hoechst 33342/propidium iodide staining.

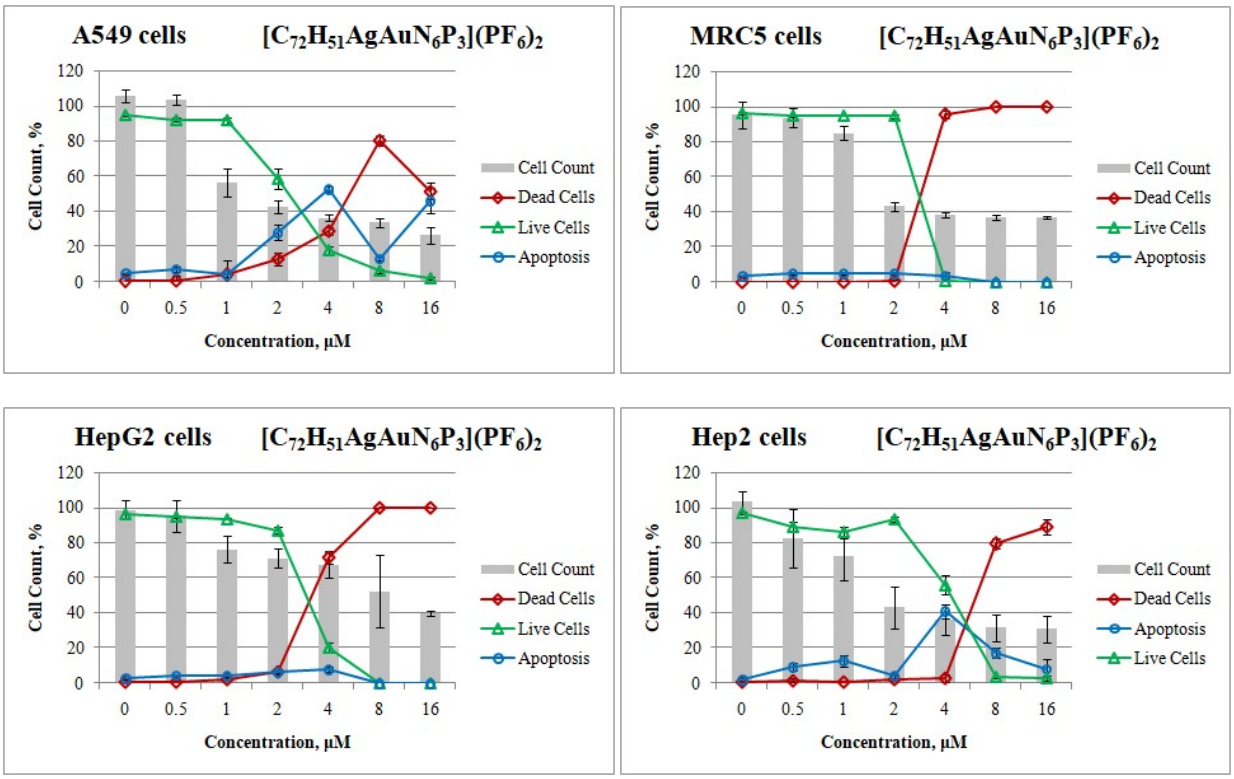

Figure S38. The effect of complex **5** on the viability of A549, MRC5, HepG2 and Hep2 cells determined after 24 h by Hoechst 33342/propidium iodide staining.

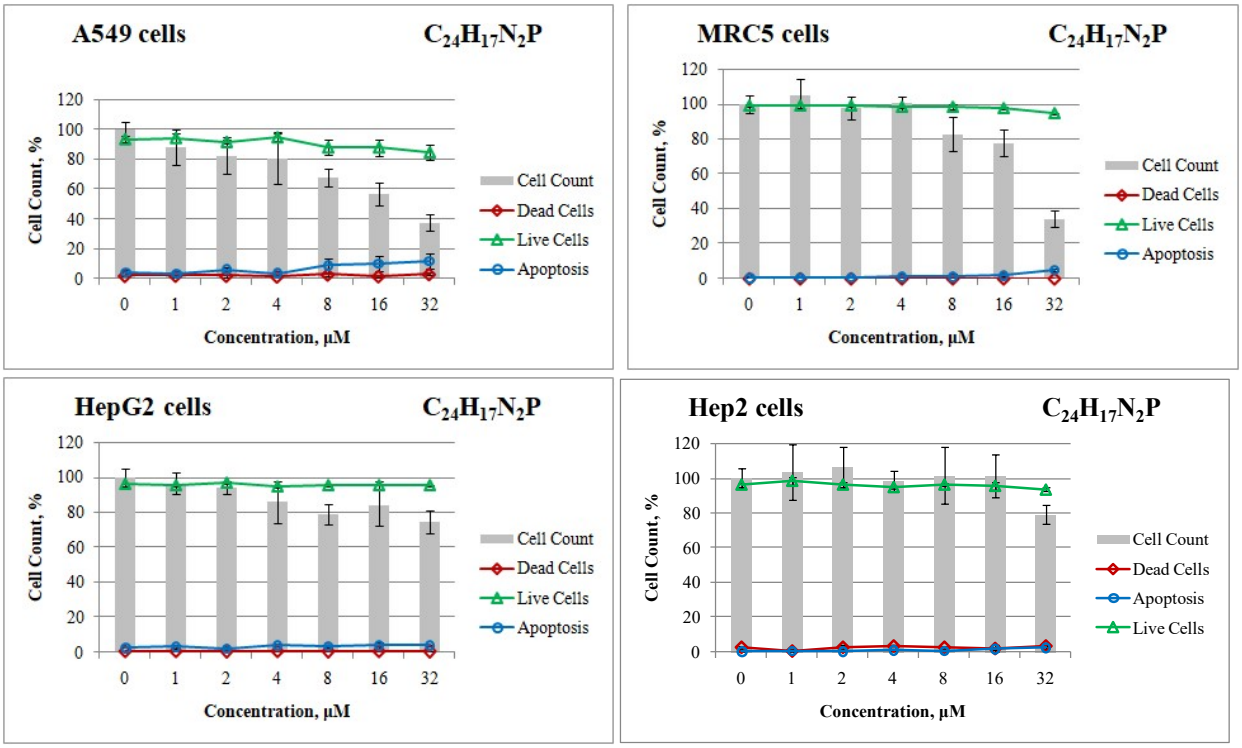

Figure S39. The effect of **L** on the viability of A549, MRC5, HepG2 and Hep2 cells determined after 24 h by Hoechst 33342/propidium iodide staining.

§9. References

1. R. Uson, A. Laguna, M. Laguna, D. A. Briggs, H. H. Murray and J. P. Fackler Jr., in *Inorg. Synth.*, 1989, 85−91.
2. *SADABS, v. 2008-1, Bruker AXS, Madison, WI, USA*, 2008.
3. G. Sheldrick, *Acta Crystallogr. A*, 2015, **71**, 3−8.
4. G. Sheldrick, *Acta Crystallogr. C*, 2015, **71**, 3−8.
5. D. A. Pantazis, X. Y. Chen, C. R. Landis and F. Neese, *J. Chem. Theory Comput.*, 2008, **4**, 908−919.
6. C. van Wüllen, *J. Chem. Phys.*, 1998, **109**, 392−399.
7. E. v. Lenthe, E. J. Baerends and J. G. Snijders, *J. Chem. Phys.*, 1993, **99**, 4597−4610.
8. R. F. W. Bader and R. F. Bader, *Atoms in Molecules: A Quantum Theory*, Clarendon Press, 1990.
9. T. Lu, *J. Chem. Phys.*, 2024, **161**, 082503.
10. A. D. Becke, *J. Chem. Phys.*, 1993, **98**, 1372−1377.
11. E. Caldeweyher, S. Ehlert, A. Hansen, H. Neugebauer, S. Spicher, C. Bannwarth and S. Grimme, *J. Chem. Phys.*, 2019, **150**, 154122.
12. T. Yanai, D. P. Tew and N. C. Handy, *Chem. Phys. Lett.*, 2004, **393**, 51−57.
13. F. Weigend and R. Ahlrichs, *Phys. Chem. Chem. Phys.*, 2005, **7**, 3297−3305.
14. F. Neese, F. Wennmohs, U. Becker and C. Riplinger, *J. Chem. Phys.*, 2020, **152**, 224108.
15. S. Hirata and M. Head-Gordon, *Chem. Phys. Lett.*, 1999, **314**, 291−299.
16. J. Tomasi and M. Persico, *Chem. Rev.*, 1994, **94**, 2027−2094.
17. Y.-J. Lee and E. Shacter, *J. Biol. Chem.*, 1999, **274**, 19792−19798.